INTERNATIONAL JOURNAL FOR NUMERICAL METHODS IN FLUIDS, VOL. 9, 891–920 (1989)

NUMERICAL SIMULATION AND HYDRODYNAMIC VISUALIZATION OF TRANSIENT VISCOUS FLOW AROUND AN OSCILLATING AEROFOIL

O. DAUBE, L. TA PHUOC AND A. DULIEU
LIMSI, BP 30, F-91406 Orsay Cedex, France

AND

M. COUTANCEAU, K. OHMI AND A. TEXIER
Laboratoire de Mécanique des Fluides, Université de Poitiers, F-86022 Poitiers, France

SUMMARY

Unsteady viscous flow around a large-amplitude and high-frequency oscillating aerofoil is examined in this paper by numerical simulation and experimental visualization. The numerical method is based on the combination of a fourth-order Hermitian finite difference scheme for the stream function equation and a classical second-order scheme to solve the vorticity transport equation. Experiments are carried out by a traditional visualization method using solid tracers suspended in water. The comparison between numerical and experimental results is found to be satisfactory. Time evolutions of the flow structure are presented for Reynolds numbers of 3×10^3 and 10^4. The influence of the amplitude and frequency of the oscillating motion on the dynamic stall is analysed.

KEY WORDS Transient flows Oscillating aerofoil Dynamic stall Navier–Stokes equations Finite differences

INTRODUCTION

The flow around an oscillating aerofoil has been for a long time one of the main interests of those concerned with unsteady separation and dynamic stall. If the angle of attack of an aerofoil oscillates around the static stall angle, large hysteresis develops in the aerodynamic force and moments. A great deal of research has been carried out on this phenomenon during the last decade, mostly in the form of wind tunnel and water tunnel experiments. A description of the mechanism of dynamic stall in the case of pitching aerofoil can be found in Ham[1] and Martin *et al.*[2] The transient forces and moments are fundamentally different from their static counterparts and cannot be reproduced when neglecting the unsteady motion. Theoretical works on the subject fall into two main classes.

The first one is based on potential flow with or without boundary layer interaction. In such a method some parameters have to be determined from experimental measurements. These methods are highly empirical and are similar to identification methods. Ham[1] and Baudu *et al.*[3] tried to model the main vortex-shedding process with potential vortices. However, these methods are not complete in the sense that some assumptions have to be made on the separation point: location, instant of appearance, incidence of the aerofoil. Unsteady boundary layer analysis gives

0271–2091/89/080891–30$15.00

Received 25 May 1988

some qualitative information on the dynamic stall delay and hysteresis but is not able to give insight into the initial vortex formation and the start of the dynamic stall.

The second class is the numerical resolution of the full unsteady Navier–Stokes equations. The inherent limitations of potential theory and boundary layer theory can be overcome by using the Navier–Stokes equations. Unless special modelling is used, this approach is limited to laminar and transitional flows. Metha[4] has studied the problem of a pitching oscillating NACA0012 aerofoil for Reynolds numbers up to 10^4. Kinney and Cielak[5] and Wu and Sampath[6] have considered the same problem but for lower Reynolds numbers. These calculations are generally limited to low reduced frequency, low mean incidence and low oscillating amplitude.

Besides these theoretical and numerical investigations, some experimental visualizations were achieved by Werlé and Gallon[7] and more recently by Ohmi and co-workers.[8,9] Another important experimental work on this subject was carried out by Carr *et al.*[10] Their analysis of the stall hysteresis, although not entirely quantitative, presents some of the most important phenomena concerning the initiation of the dynamic stall and the effect of the main experimental parameters.

The aim of this paper is to analyse with the help of both numerical simulation and experimental visualization the unsteady separation around an oscillating aerofoil at high angle of attack, high reduced frequency and high amplitude of oscillation. A comparison between the numerical results and the experimental visualizations is reported and shows good agreement.

PHYSICAL EQUATIONS

Definition of the motion

Throughout this study the pitching motion of the aerofoil will be defined by the angle of attack

$$\alpha = \bar{\alpha} + \Delta\alpha \cdot \cos(2\pi \tilde{f} \cdot \tilde{t})$$

where $\tilde{t}$ is the physical time and $\tilde{f}$ is the frequency of the oscillation. The pitching axis is located either at the half-chord or at a third-chord from the leading edge. The aerofoil is placed in an incoming flow with uniform velocity U_∞ at infinity.

We are interested in the the transient flow generated by the impulsively started translating and oscillating motions of the aerofoil.

Governing equations

All the variables are made dimensionless with respect to the half-chord $c/2$ of the aerofoil and the uniform velocity of the flow at infinity, U_∞. The main non-dimensional parameters of the flow are:

Reynolds number	Re	$= U_\infty c/\nu$
reduced frequency	f	$= \tilde{c}\tilde{f}/2U_\infty$
mean incidence	$\bar{\alpha}$	
Amplitude of the oscillation	$\Delta\alpha$	
reduced time	t	$= 2U_\infty \tilde{t}/c.$

In an inertial frame of reference Oxy translating with the aerofoil (see Figure 1), the Navier–Stokes equations in vorticity function ω_1 and streamfunction Ψ_1 formulation are

$$\frac{Re}{2}\left(\frac{\partial \omega_1}{\partial t}+\nabla\cdot(\omega_1 \mathbf{V}_1)\right)=\nabla^2\omega_1, \tag{1}$$

$$\nabla^2\Psi=\omega_1, \tag{2}$$

where $\omega_1\mathbf{k}=\nabla\times\mathbf{V}_1$, $\mathbf{V}_1=\mathbf{k}\times\nabla\Psi_1$, $\mathbf{V}_1$ is the velocity and $\mathbf{k}$ is the unit vector orthogonal to the Oxy plane.

Let Oxy be a frame of reference which rotates with the aerofoil. Let Ω be the angular velocity, $\mathbf{V}$ be the relative velocity in Oxy and ω be the relative vorticity. Then

$$\mathbf{V}_1=\mathbf{V}+\boldsymbol{\Omega}\times\mathbf{r}, \qquad \omega_1=\omega+2\Omega.$$

The relative stream function Ψ is defined by

$$\Psi_1=\Psi+\Omega r^2/2.$$

The vorticity transport equation (1) becomes

$$\frac{Re}{2}\left(2\frac{d\Omega}{dt}+\frac{\partial\omega}{\partial t}+\nabla\cdot(\omega\mathbf{V})\right)=\nabla^2\omega \tag{3}$$

and the streamfunction Ψ satisfies

$$\nabla^2\Psi=\omega. \tag{4}$$

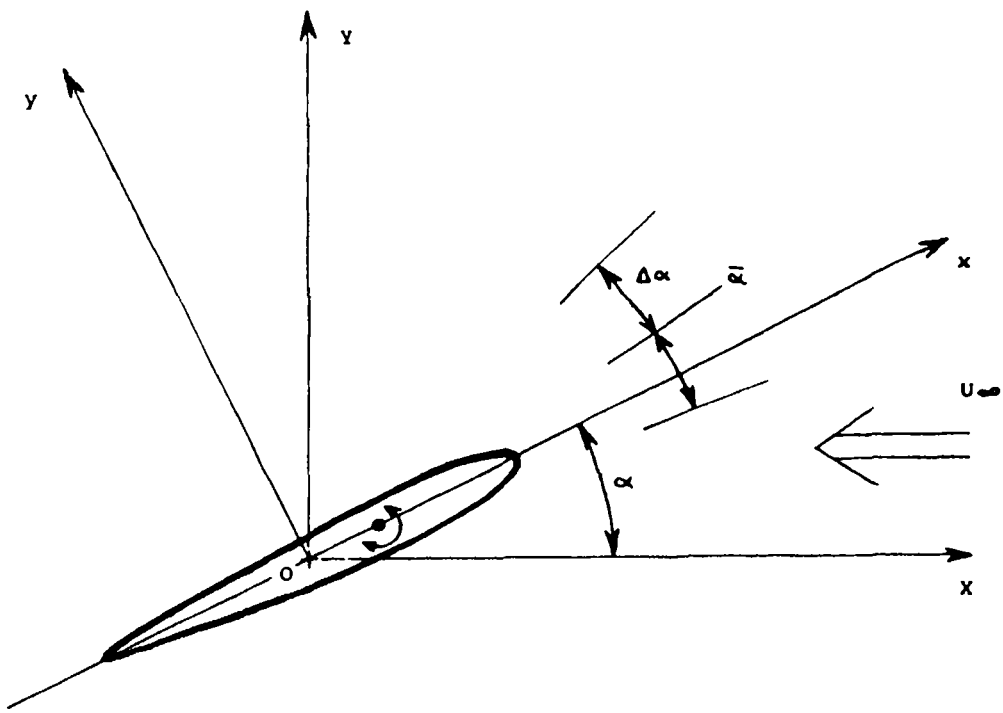

Figure 1. Sketch of the configuration

The boundary conditions for the streamfunction Ψ are

$$\nabla\Psi = \mathbf{0} \quad \text{on the aerofoil,}$$

$$\nabla\Psi \to -\mathbf{i} + \Omega\mathbf{k} \times \mathbf{r} \quad \text{when } r^2 = x^2 + y^2 \to \infty.$$

The initial conditions are those of an impulsively started motion.

The calculations are actually done in the rotating frame Oxy, using the functions Ψ_1 and ω_1 in order to avoid large values of Ψ when $r \to \infty$. The Navier–Stokes equations then read:

$$\frac{Re}{2}\left\{\frac{\partial\omega_1}{\partial t} + \frac{\partial}{\partial y}\left[\omega_1 \frac{\partial}{\partial x}\left(\Psi_1 - \frac{\Omega r^2}{2}\right)\right] - \frac{\partial}{\partial x}\left[\omega_1 \frac{\partial}{\partial y}\left(\Psi_1 - \frac{\Omega r^2}{2}\right)\right]\right\} = \nabla^2\omega_1, \tag{5}$$

$$\nabla^2\Psi_1 = \omega_1. \tag{6}$$

TRANSFORMED EQUATIONS

The domain outside the aerofoil in the rotating plane $z = x + iy$ is mapped by a conformal mapping onto the exterior of a circular cylinder, which in turn is mapped by the exponential mapping onto a semi-infinite strip $[0, \infty[\times [0, 2]$ in a plane $\zeta = \xi + i\eta$:

$$z = \exp(\pi\zeta) + \gamma + \frac{\varepsilon^2}{\exp(\pi\zeta) + \gamma} - \sigma,$$

where σ defines the location of the pitch axis and ε defines the thickness of the aerofoil. The line $\xi = 0$ in the computational plane represents the aerofoil wall.

Let $h^2(\xi, \eta)$ be the conformal mapping modulus. In the (ξ, η)-plane the Navier–Stokes equations are

$$\frac{Re}{2}\left\{h^2\frac{\partial\omega_1}{\partial t} + \frac{\partial}{\partial\eta}\left[\omega_1 \frac{\partial}{\partial\xi}\left(\Psi_1 - \frac{\Omega r^2}{2}\right)\right] - \frac{\partial}{\partial\xi}\left[\omega_1 \frac{\partial}{\partial\eta}\left(\Psi_1 - \frac{\Omega r^2}{2}\right)\right]\right\} = \nabla^2_{\xi,\eta}\omega_1, \tag{7}$$

$$\nabla^2_{\xi,\eta}\Psi_1 = h^2\omega_1, \tag{8}$$

where $\nabla^2_{\xi,\eta}$ stands for $\partial^2/\partial\xi^2 + \partial^2/\partial\eta^2$.

Boundary conditions

On the surface of the aerofoil the no-slip condition is the only available physical condition:

$$\text{on } \xi = 0 \quad \begin{cases} \dfrac{\partial\Psi_1}{\partial\eta} = \dfrac{\partial}{\partial\eta}\left(\dfrac{\Omega r^2}{2}\right), \\ \dfrac{\partial\Psi_1}{\partial\xi} = \dfrac{\partial}{\partial\xi}\left(\dfrac{\Omega r^2}{2}\right). \end{cases} \tag{9}$$

In view of the fourth-order compact scheme which will be used to solve the Poisson equation of the streamfunction, numerical boundary conditions for Ψ and its second derivative on the wall are needed. These conditions are derived from (9), which allows us to set $\Psi = 0$ on the wall, and

from the Poisson equation written on the surface of the aerofoil:

$$\text{on } \xi=0 \begin{cases} \dfrac{\partial^2 \Psi_I}{\partial \eta^2} = \dfrac{\partial}{\partial \eta^2}\left(\dfrac{\Omega r^2}{2}\right), \\ \dfrac{\partial^2 \Psi_I}{\partial \xi^2} = h^2 \omega_I - \dfrac{\partial^2 \Psi_I}{\partial \eta^2}, \\ \Psi_I = \dfrac{\Omega r^2}{2}. \end{cases} \tag{10}$$

At infinity the computational domain has to be limited in the ξ-direction. So, at a sufficiently long distance ξ_∞ of the aerofoil, the flow is assumed to be irrotational almost everywhere, except in a downstream area where open boundary conditions have to be set in order to enable the wake to flow through this artificial boundary. In a previous paper by Ta Phuoc and Bouard[11] such a condition has been established: the viscous effects are assumed to be negligible compared with the convective one, which requires the vanishing of the total derivative of the vorticity ω_I on $\xi=\xi_\infty$:

$$\frac{Re}{2}\left\{h^2\frac{\partial \omega_I}{\partial t}+\frac{\partial}{\partial \eta}\left[\omega_I\frac{\partial}{\partial \xi}\left(\Psi_I-\frac{\Omega r^2}{2}\right)\right]-\frac{\partial}{\partial \xi}\left[\omega_I\frac{\partial}{\partial \eta}\left(\Psi_I-\frac{\Omega r^2}{2}\right)\right]\right\}=0. \tag{11}$$

A similar form has been used by Lugt and Haussling[16] in which the real velocity is replaced by the uniform velocity at infinity.

In order to get a complete set of boundary conditions, it will be assumed that at ξ_∞ the following relation holds:

$$\frac{\partial}{\partial \xi}\left[\frac{1}{h}\frac{\partial}{\partial \xi}\left(\Psi_I-\frac{\Omega r^2}{2}\right)\right]=0. \tag{12}$$

This relation means that the normal derivative of the inertial tangential velocity is assumed to vanish at $\xi=\xi_\infty$. In the part of the outer boundary outside the wake the values of the streamfunction Ψ_I and its derivatives will be deduced from the assumption of irrotational flow.

In all the computations this downstream area is defined by

$$-\pi/6 \leqslant \theta \leqslant \pi/6.$$

NUMERICAL METHOD

The numerical algorithm is a combination of two schemes: a fourth-order compact scheme for the resolution of the Poisson equation and a second-order scheme for the resolution of the vorticity transport equation. It was proposed by Ta Phuoc, Daube and co-workers[11,13,14] and has proved to be efficient for a large class of incompressible viscous flows.

Outline of the fourth-order compact scheme

Following Hirsh,[15] the fourth-order accuracy is achieved by 'compact' relations relating the values of a function and its derivatives on a three-point stencil. In counterpart, it is necessary to introduce the second derivatives of Ψ as supplementary unknowns. This scheme is based upon the following relations.

Let Δx be the constant spatial discretization step and let f_i, f'_i, f''_i be the values of the function f and its derivatives at node i. The following tridiagonal relations hold:

$$f'_{i-1}+4f'_i+f'_{i+1}=\frac{3}{\Delta x}(f_{i+1}-f_{i-1})+O(\Delta x^4), \tag{13}$$

$$f''_{i-1}+10f''_i+f''_{i+1}=\frac{12}{\Delta x^2}(f_{i+1}-2f_i+f_{i-1})+O(\Delta x^4). \tag{14}$$

The knowledge of Ψ_I and its second derivatives from relation (10) on the boundaries enables us to use these relations.

The combination of the Poisson equation (8) and the relation (14) yields a linear system which is solved by means of an ADI algorithm for elliptic equations.[16] The two half-steps of the kth iteration of the ADI procedure are given below.

First half-step

$$\lambda_{k\eta}\Psi^{k*}_{I_{ij}}-\left(\frac{\partial^2\Psi_I}{\partial\eta^2}\right)^{k*}_{ij}=-h_{ij}\omega^{n+1}_{I_{ij}}+\left(\frac{\partial^2\Psi_I}{\partial\xi^2}\right)^{k}_{ij}+\lambda_{k\eta}\Psi^{k}_{I_{ij}}, \tag{15}$$

$$\frac{12}{\Delta\eta^2}(\Psi^{k*}_{I_{ij+1}}-2\Psi^{k*}_{I_{ij}}+\Psi^{k*}_{I_{ij-1}})-\left[\left(\frac{\partial^2\Psi_I}{\partial\eta^2}\right)^{k*}_{ij+1}+10\left(\frac{\partial^2\Psi_I}{\partial\eta^2}\right)^{k*}_{ij}+\left(\frac{\partial^2\Psi_I}{\partial\eta^2}\right)^{k*}_{ij-1}\right]=0. \tag{16}$$

Second half-step

$$\lambda_{k\xi}\Psi^{k+1}_{I_{ij}}-\left(\frac{\partial^2\Psi_I}{\partial\xi^2}\right)^{k+1}_{ij}=-h_{ij}\omega^{n+1}_{I_{ij}}+\left(\frac{\partial^2\Psi_I}{\partial\eta^2}\right)^{k*}_{ij}+\lambda_{k\xi}\Psi^{k*}_{I_{ij}}, \tag{17}$$

$$\frac{12}{\Delta\xi^2}(\Psi^{k+1}_{I_{i+1j}}-2\Psi^{k+1}_{I_{ij}}+\Psi^{k+1}_{I_{i-1j}})-\left[\left(\frac{\partial^2\Psi_I}{\partial\xi^2}\right)^{k+1}_{i+1j}+10\left(\frac{\partial^2\Psi_I}{\partial\xi^2}\right)^{k+1}_{ij}+\left(\frac{\partial^2\Psi_I}{\partial\xi^3}\right)^{k+1}_{i-1j}\right]=0. \tag{18}$$

The coefficients $\lambda_{k\eta}$ and $\lambda_{k\xi}$ are optimum convergence parameters and were proposed by Wachspress.[16]

Once the values of the streamfunction Ψ_I are known, the values of its first derivatives are calculated through the use of the relation (13) together with boundary conditions (9). These calculations involve only the resolution of tridiagonal systems.

Vorticity transport equation

A second-order-accurate scheme has been chosen to solve this equation. This choice is motivated by the difficulties which arise when trying to use a fourth-order compact scheme as in the case of the Poisson equation of the streamfunction. In fact no physical boundary conditions are available for the vorticity and *a fortiori* for its first and second derivatives. Moreover, it is possible with a second-order scheme to use the conservative form of the transport equation. The time-marching procedure is a classical Peaceman–Racheford one. Each time step is split into two half-steps. Integration in the η-direction is performed during the first half-step and integration in the ξ-direction during the second half-step. Let n and $n+1$ be superscripts denoting the values of variables at time $n\Delta t$ and $(n+1)\Delta t$ respectively. Using centred differences, the two half-steps are written as below.

First half-step

$$Re\frac{h_{ij}}{\Delta t}\omega_{1_{ij}}^{n*} - \frac{\omega_{1_{ij+1}}^{n*} - 2\omega_{1_{ij}}^{n*} + \omega_{1_{ij-1}}^{n*}}{\Delta\eta^2} + \frac{Re}{4}\frac{(v^n\omega_1^{n*})_{ij+1} - (v^n\omega_1^{n*})_{ij-1}}{\Delta\eta}$$

$$= Re\frac{h_{ij}}{\Delta t}\omega_{1_{ij}}^{n} + \frac{\omega_{1_{i+1j}}^{n} - 2\omega_{1_{ij}}^{n} + \omega_{1_{i-1j}}^{n}}{\Delta\xi^2} + \frac{Re}{4}\frac{(u^n\omega_1^n)_{i+1j} - (u^n\omega_1^n)_{i-1j}}{\Delta\xi}. \tag{19}$$

The η-direction being the 'tangential' one, the boundary conditions which are used for the vorticity are derived from the periodicity condition

$$\omega(0,\xi) = \omega(2,\xi) \quad \forall\xi.$$

Second half-step

$$Re\frac{h_{ij}}{\Delta t}\omega_{1_{ij}}^{n+1} - \frac{\omega_{1_{i+1j}}^{n+1} - 2\omega_{1_{ij}}^{n+1} + \omega_{1_{i-1j}}^{n+1}}{\Delta\xi^2} + \frac{Re}{4}\frac{(u^n\omega_1^{n+1})_{i+1j} - (u^n\omega_1^{n+1})_{i-1j}}{\Delta\xi}$$

$$= Re\frac{h_{ij}}{\Delta t}\omega_{1_{ij}}^{n*} + \frac{\omega_{1_{ij+1}}^{n*} - 2\omega_{1_{ij}}^{n*} + \omega_{1_{ij-1}}^{n*}}{\Delta\eta^2} - \frac{Re}{4}\frac{(v^n\omega_1^{n*})_{ij+1} - (v^n\omega_1^{n*})_{ij-1}}{\Delta\eta}, \tag{20}$$

where

$$u = -\frac{\partial}{\partial\eta}\left(\Psi_1 - \frac{\Omega r^2}{2}\right), \qquad v = \frac{\partial}{\partial\xi}\left(\Psi_1 - \frac{\Omega r^2}{2}\right).$$

On the aerofoil the so-called Woods condition is used:

$$2h^2(0,\eta)\omega(0,\eta) + h^2(\Delta\xi,\eta)g(\Delta\xi,\eta) = \frac{6}{\Delta\xi^2}[\Psi(\Delta\xi,\eta) - \Psi(0,\eta)] + O(\Delta\xi^2).$$

At infinity, for points outside the downstream area defined earlier, the flow is assumed to be irrotational, i.e. $\omega(\xi_\infty,\eta) = 0$, while in the downstream area the relation (11) is used.

EXPERIMENTAL ARRANGEMENTS

The visualization experiments were conducted in a vertical tank with a square cross-section ($90 \times 90 \times 180$ cm^3). The tracers are thin macromolecular particles called Rilsan. The advantage of using these particles lies in the fact that less problems arise for the orientation of reflection than with aluminium particles. The representative size of a particle is between 80 and 200 μm. The motion of the tracers is visualized by a sheet of intense arc light which illuminates the median vertical cross-section of the tank. The aerofoil translates vertically in the tank and its speed is controlled by a hydraulic driving device which is connected to a variable resistance dash pot. The camera is fixed to a carriage which translates at the aerofoil speed. Thus the visualizations are made in the inertial frame translating with the aerofoil. An electric winding device enables photographs to be made at regular time intervals. The pitch oscillation is generated by a connecting rod mechanism via which the rotation of a pulley, coupled with the translation of the carriage, is transformed into the desired motion. The angular displacement is a sinusoidal function of time.

RESULTS AND DISCUSSION

The aerofoil which has been considered is a NACA0012 aerofoil pitching around an axis located at a third-chord from the leading edge. The calculations have been achieved for two values of the

Reynolds number, $Re = 3 \times 10^3$ and 10^4. A systematic study of the influence of the different parameters of the oscillating motion on the dynamic stall development is given. All calculations are compared with experimental visualizations.

Throughout this section t^* will denote the dimensionless time normalized with respect to the chord of the aerofoil instead of the half-chord. The frequency f^* has the same definition as 'f'

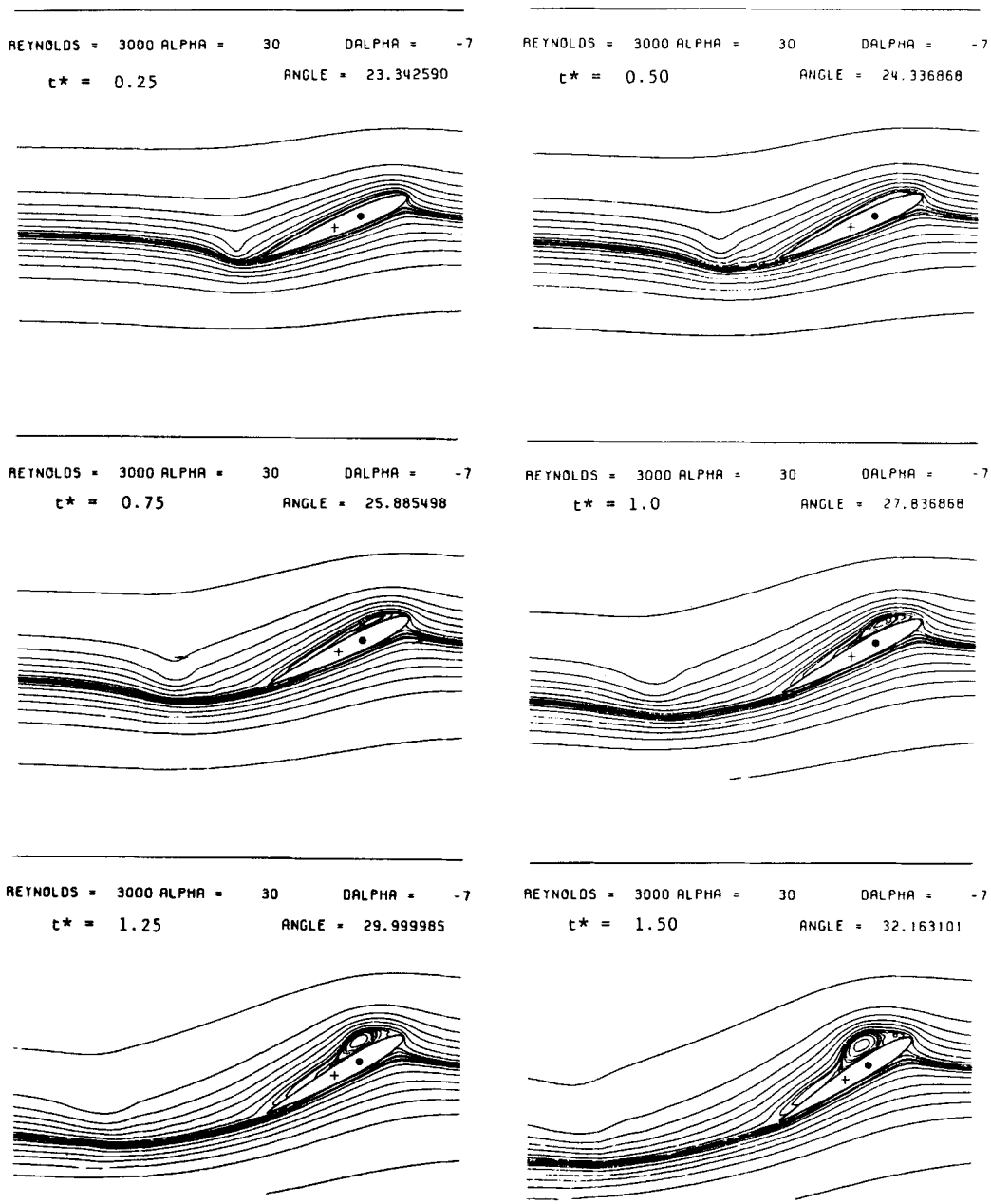

Figure 2(a)

given earlier.

$Re = 3 \times 10^3$

The characteristics of the flow past an oscillating aerofoil are mainly determined by the relative magnitude of the oscillating motion with respect to the translation rate of the incoming flow. This

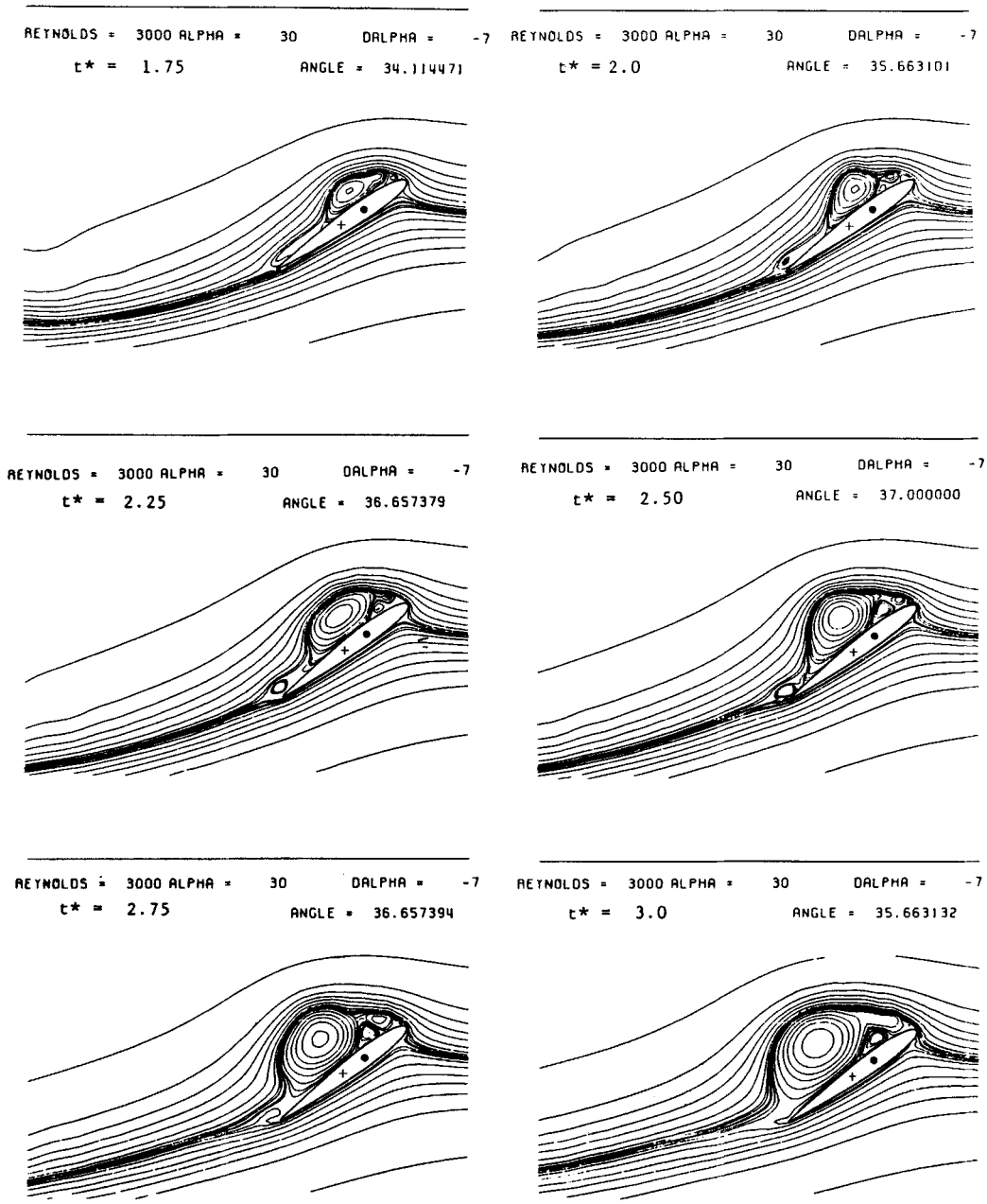

Figure 2(b)

effect can be characterized by the reduced frequency f^* and the amplitude $\Delta\alpha$. For $Re = 3 \times 10^3$ we will focus on the effects of these two parameters on the flow generation and on the onset and development of the leading edge and trailing edge vortices.

Influence of the reduced frequency f^*. Three values of the reduced frequency are considered here: $f^* = 0{\cdot}1$, $0{\cdot}5$ and 1. The mean value $\bar{\alpha}$ of the oscillating angle α is set to 30° which

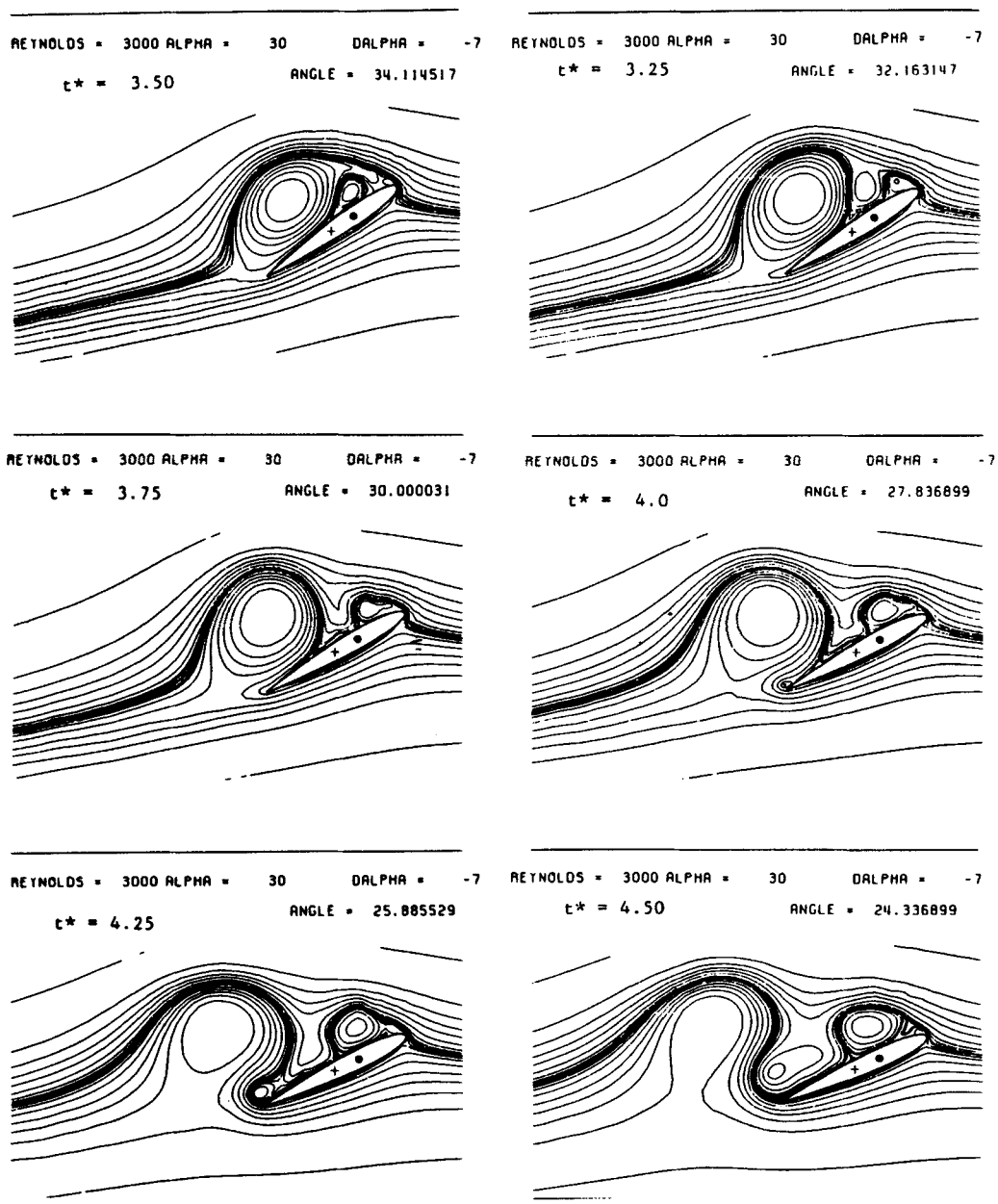

Figure 2(c)

corresponds to a deep static stall. The amplitude of the angular oscillation is 7° and the initial angle of incidence is 23°.

$f^* = 0{\cdot}1$. This reduced frequency is the lowest value which will be considered in this study. It corresponds to a low ratio between the translational velocity of the flow and the rotational

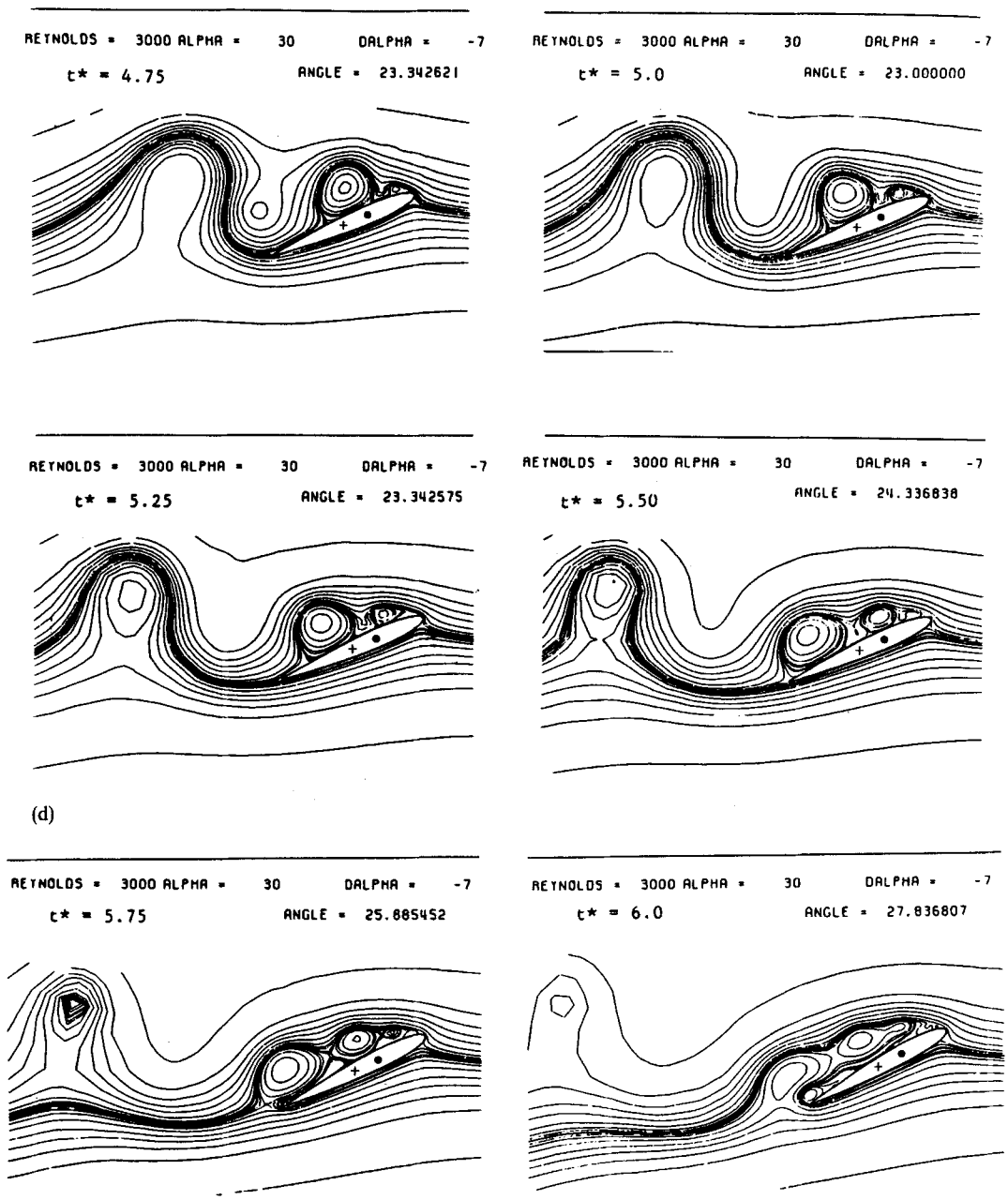

Figure 2. Time evolution of the flow structure; $Re = 3000, f^* = 0{\cdot}1, \alpha = 30°, \Delta\alpha = -7°, \xi_\infty = 0{\cdot}72324$

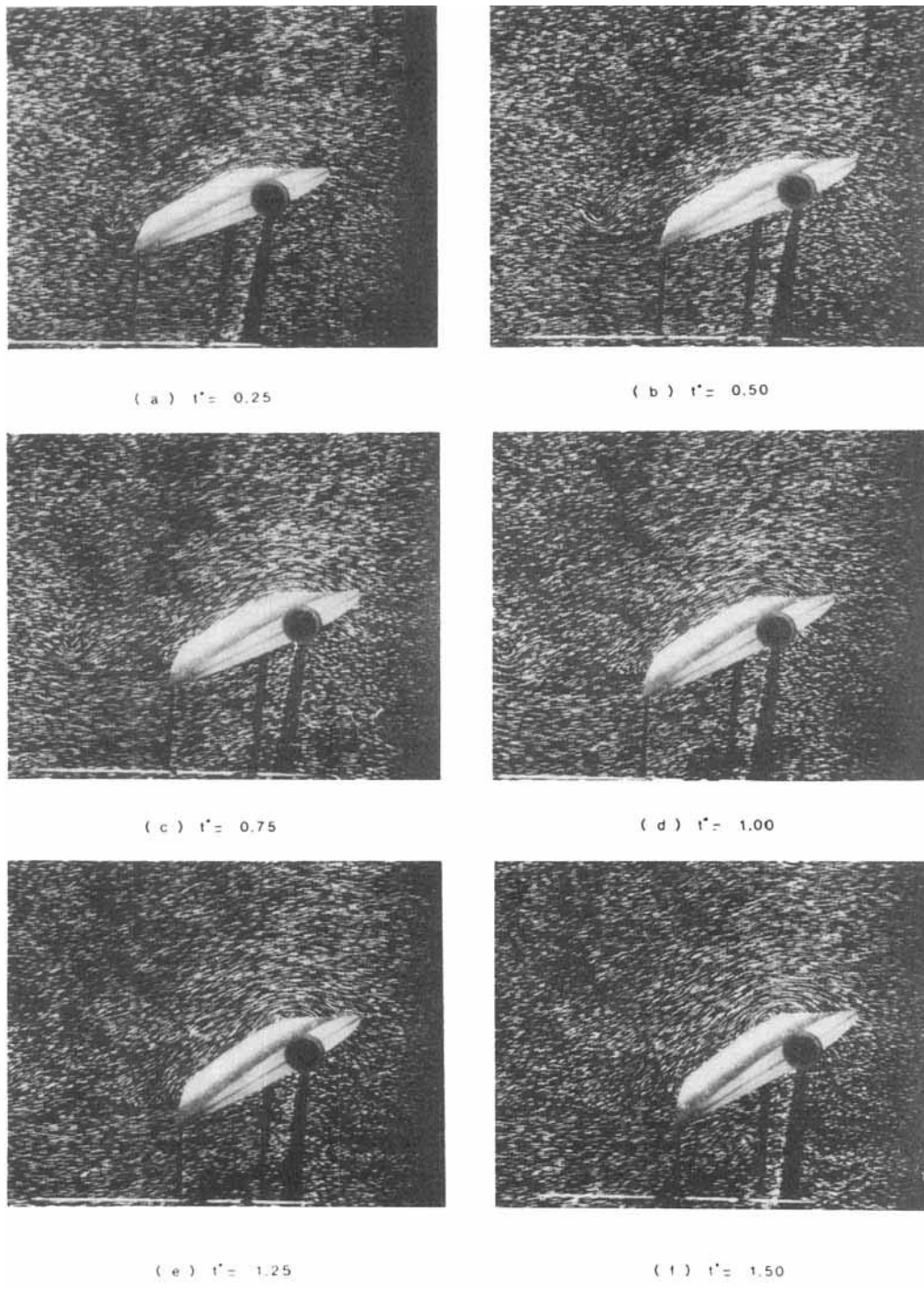

Figure 3(a)

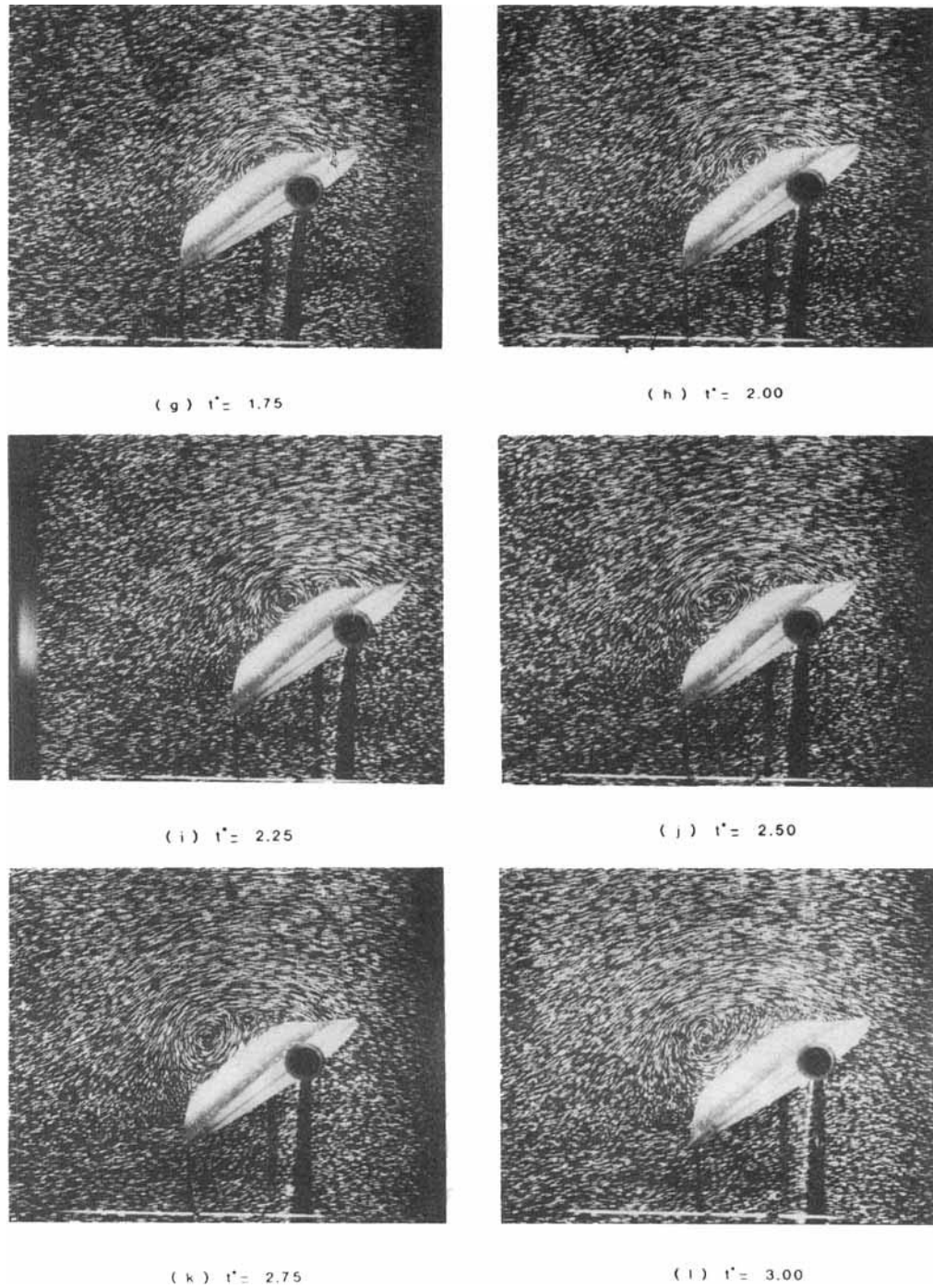

Figure 3(b)

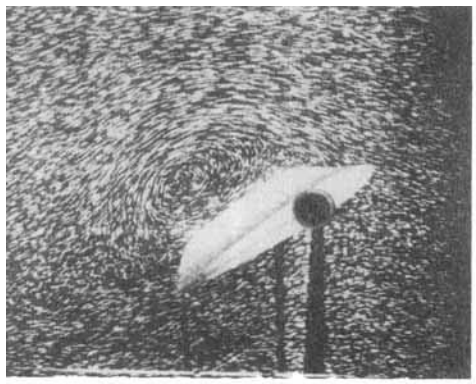

(m) t*= 3.25

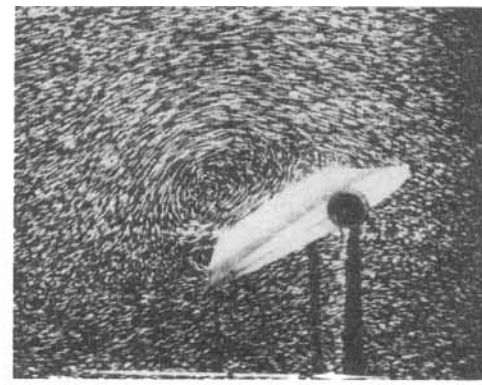

(n) t*= 3.50

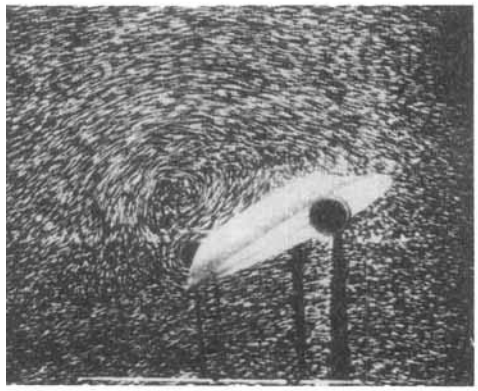

(o) t*= 3.75

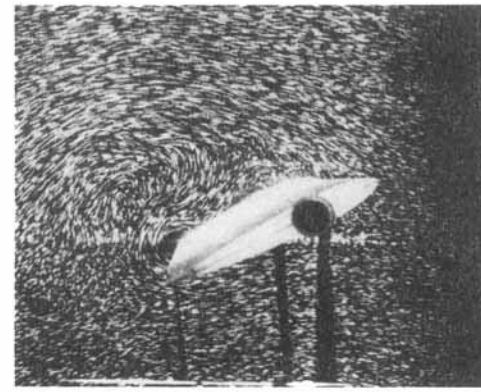

(p) t*= 4.00

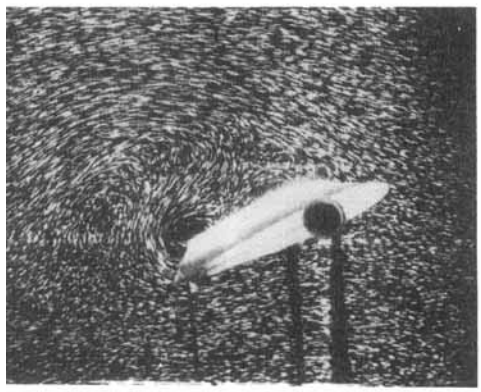

(q) t*= 4.25

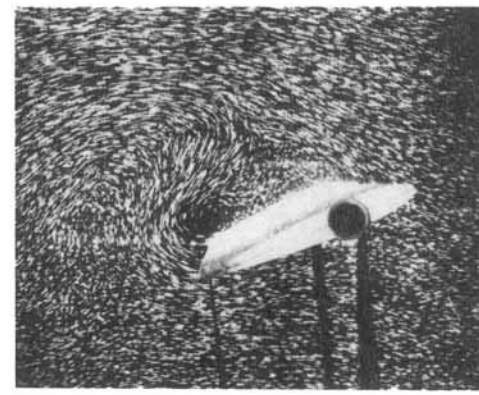

(r) t*= 4.50

Figure 3(c)

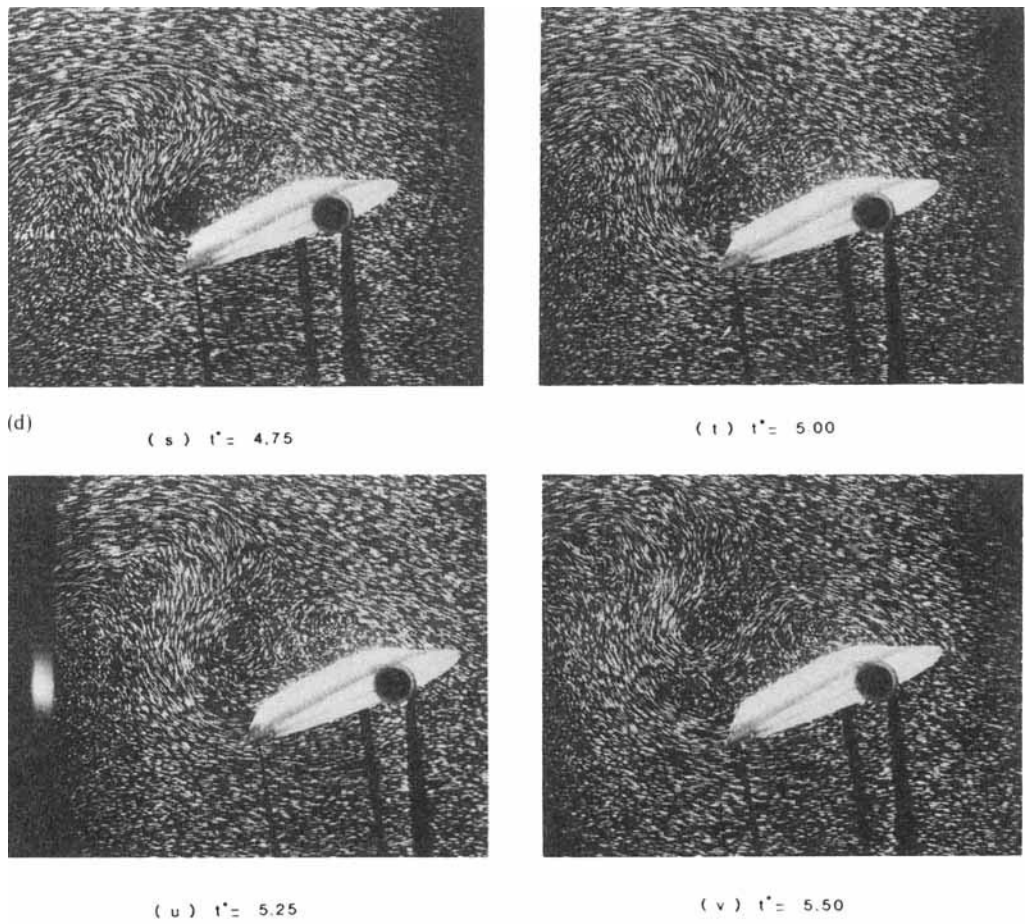

Figure 3. Time evolution of the flow structure; $Re = 3000, f^* = 0{\cdot}1, \alpha = 30^\circ, \Delta\alpha = -7^\circ, \alpha_0 = 23$

velocity of the aerofoil. The numerical solution was computed on an 81×101 grid and with a time step equal to 10^{-2}. The time evolution of the flow structure is reported in Figures 2(a)–2(d). Comparison between these results and the experimental visualizations (Figures 3(a)–3(d)) shows good agreement. For $t^* < 1$ a small separation bubble can be observed on the upper surface in the vicinity of the leading edge. This phenomenon is seen in both calculations and visualizations. The appearance of secondary vortices takes place at about $t^* = 1{\cdot}5$ in the experiments and at about $t^* = 1{\cdot}75$ in the calculations. The vortices seem slightly more developed in the visualizations than in the calculations. These discrepancies are mainly due to the grid which was used. However, it must be emphasized that all vortices seen in the visualizations are also reproduced by the numerical simulation.

$f^* = 0{\cdot}5$. This reduced frequency corresponds to a large ratio between the rotational and translational motions. The visualizations (Figures 4(a) and 4(b)) were achieved in the same experimental conditions as in the previous case. The numerical simulations were performed on the same grid but with a time step equal to 5×10^{-3} instead of 10^{-2}.

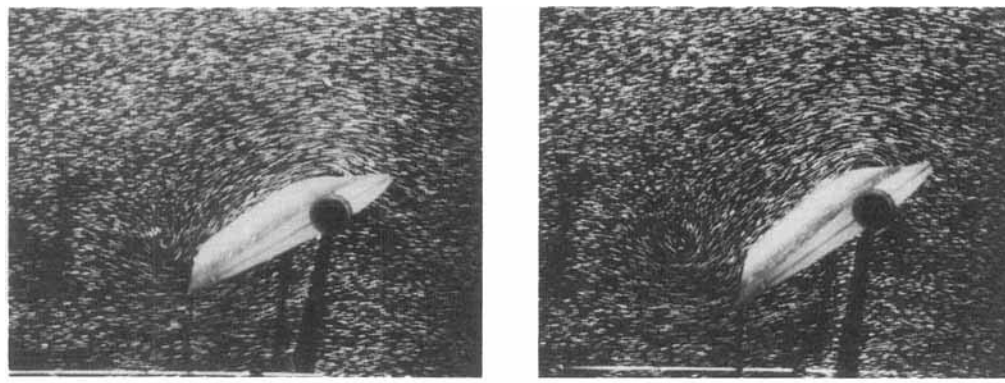

(a) t* = 0.25 (b) t* = 0.50

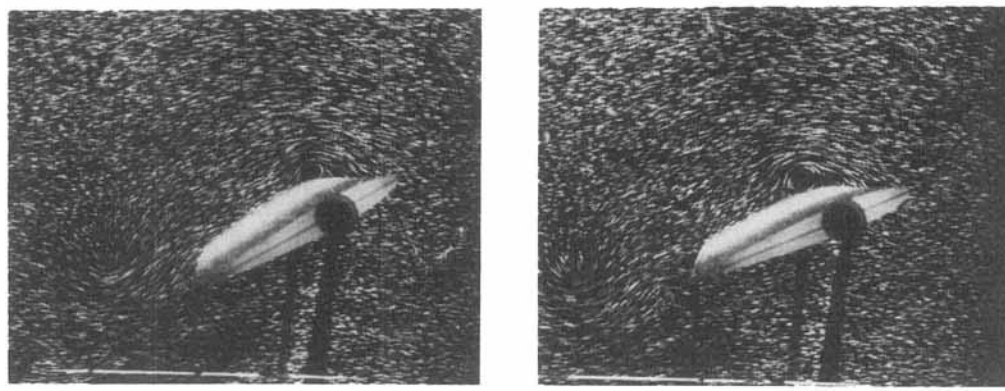

(c) t* = 0.75 (d) t* = 1.00

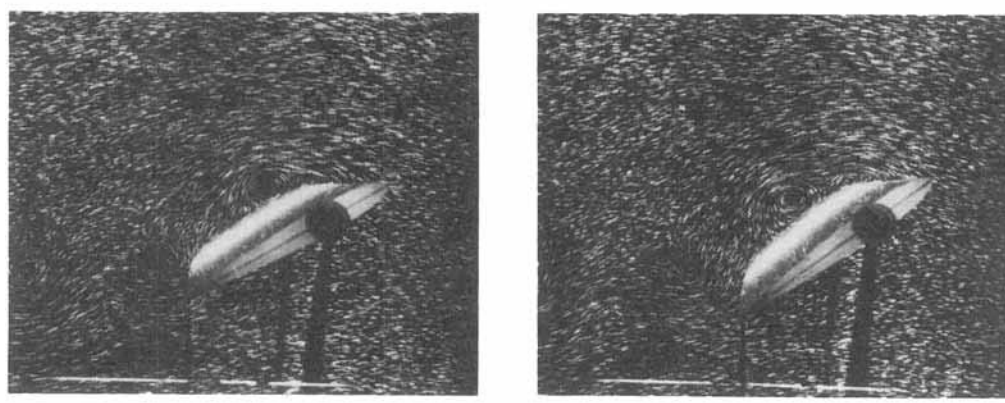

(e) t* = 1.25 (f) t* = 1.50

Figure 4(a)

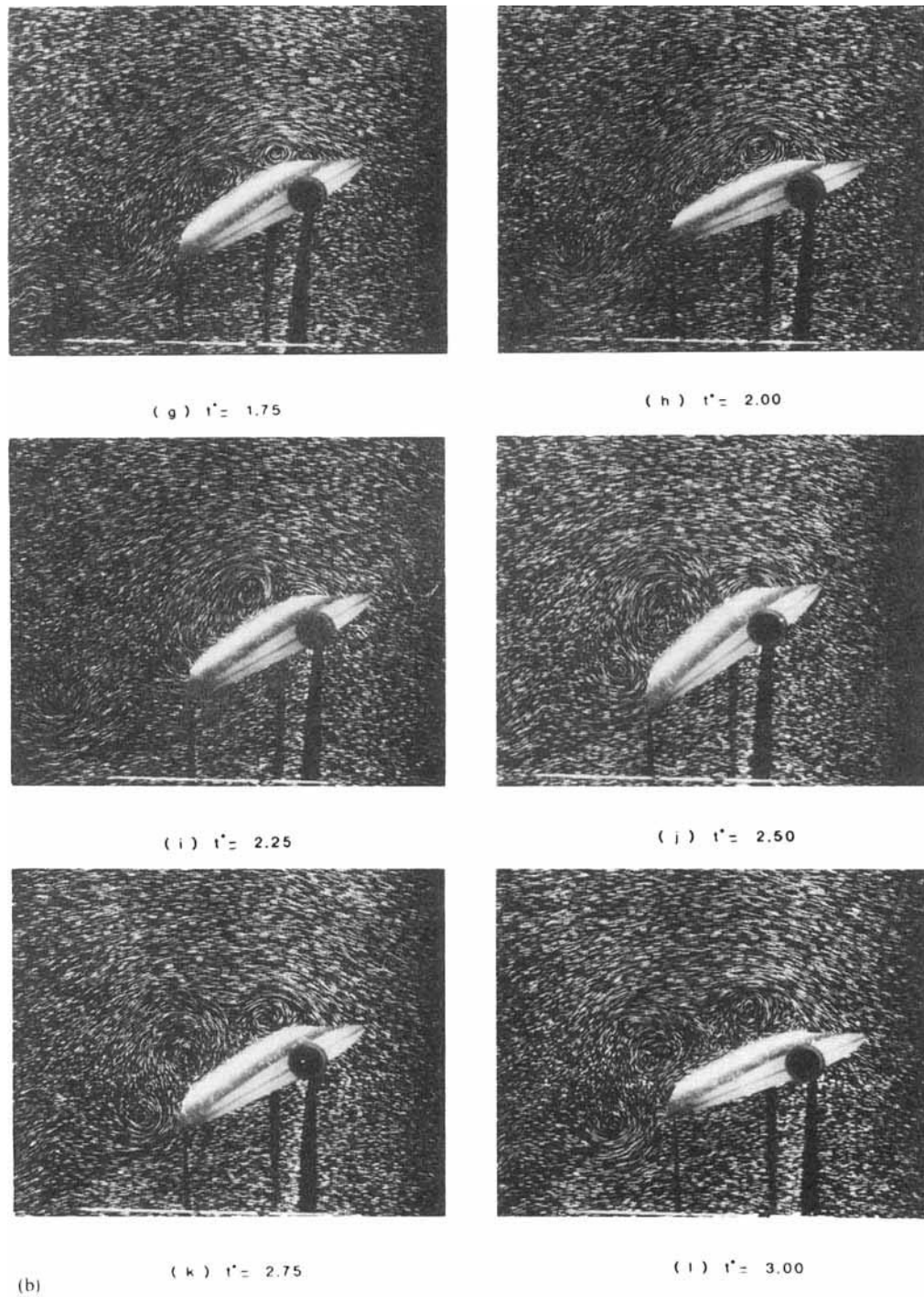

Figure 4. Time evolution of the flow structure; $Re = 3000$, $f^* = 0{\cdot}5$, $\alpha = 30^\circ$, $\Delta\alpha = -7^\circ$, $\alpha_0 = 23$

Two distinct vortex systems are shed from the leading and trailing edges. They are parallel to each other with opposite rotation. The separation zone on the upper surface is larger and more irregular than that for $f^* = 0{\cdot}1$. The trailing vortices, which are generated alternately on the upper and the lower surfaces, have a larger intensity. The frequency of these vortex sheddings is the same as the oscillation frequency. At the leading edge a vortex appears only on the upper surface. This vortex grows, moves downwards along the extrados and combines eventually with

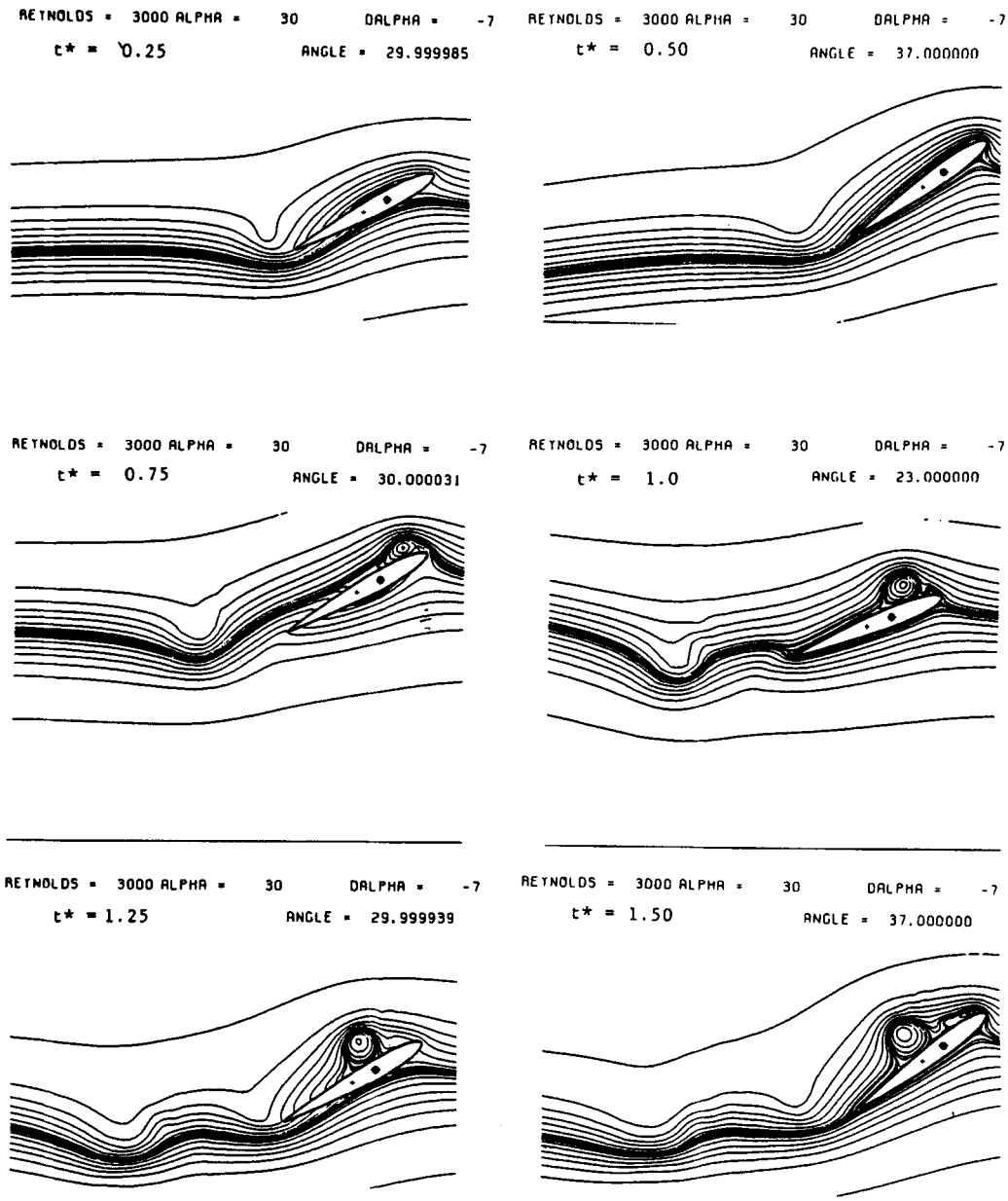

Figure 5(a)

the trailing edge vortex, giving the two vortex sheddings in the wake. These phenomena can be seen in both experimental (Figures 4(a) and 4(b)) and computational(Figures 5(a) and 5(b)) results.

$f^* = 1{\cdot}0$. In this case the velocity of the aerofoil edges is about three times that of the incoming flow. The flow structures observed in this case are similar to those obtained for $f^* = 0{\cdot}5$ but are much more irregular. Vortices appear alternately on the upper and the lower parts of the leading

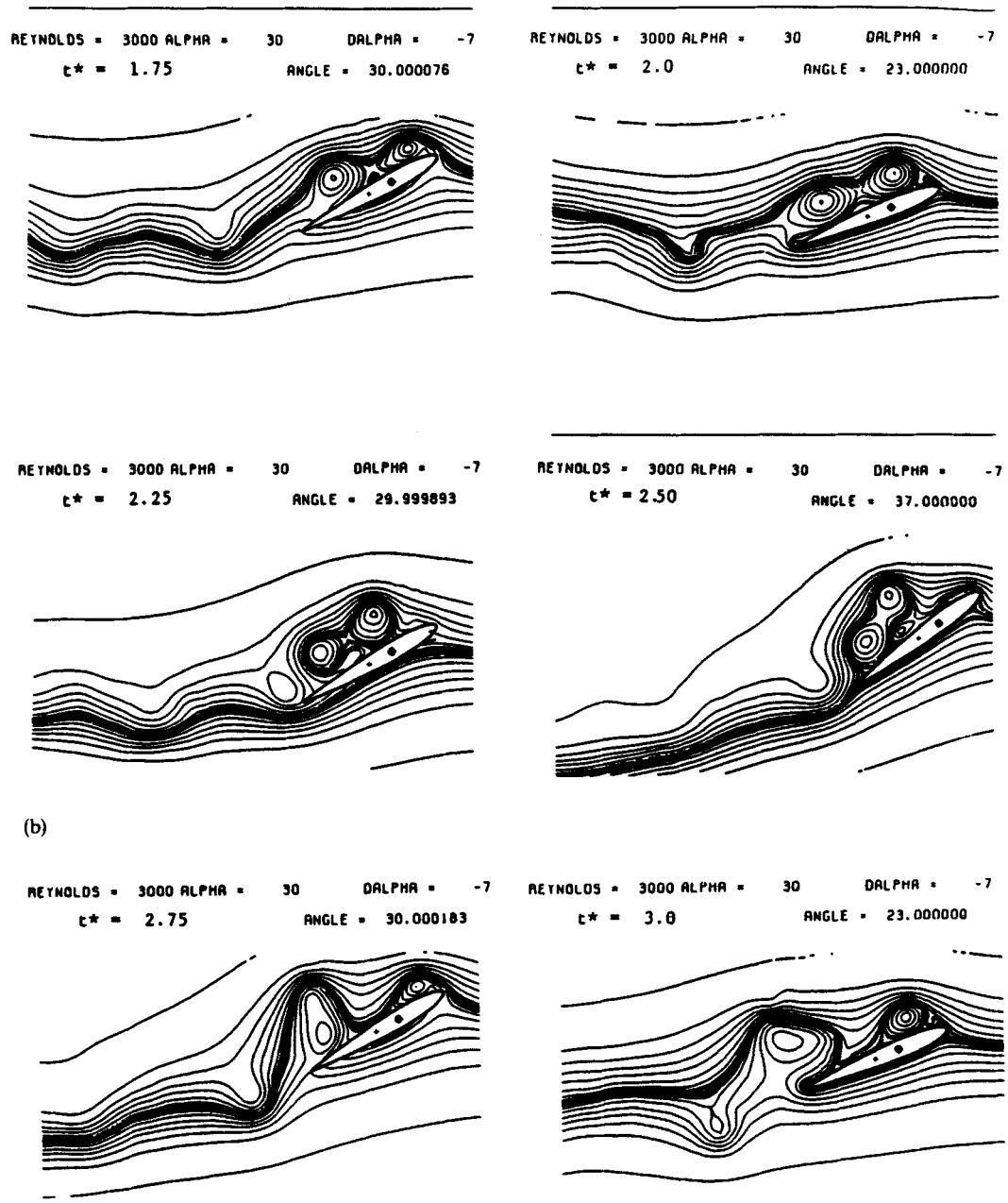

Figure 5. Time evolution of the flow structure; $Re = 3000, f^* = 0{\cdot}5, \alpha = 30°, \Delta\alpha = -7°, \xi_\infty = 0{\cdot}72324$

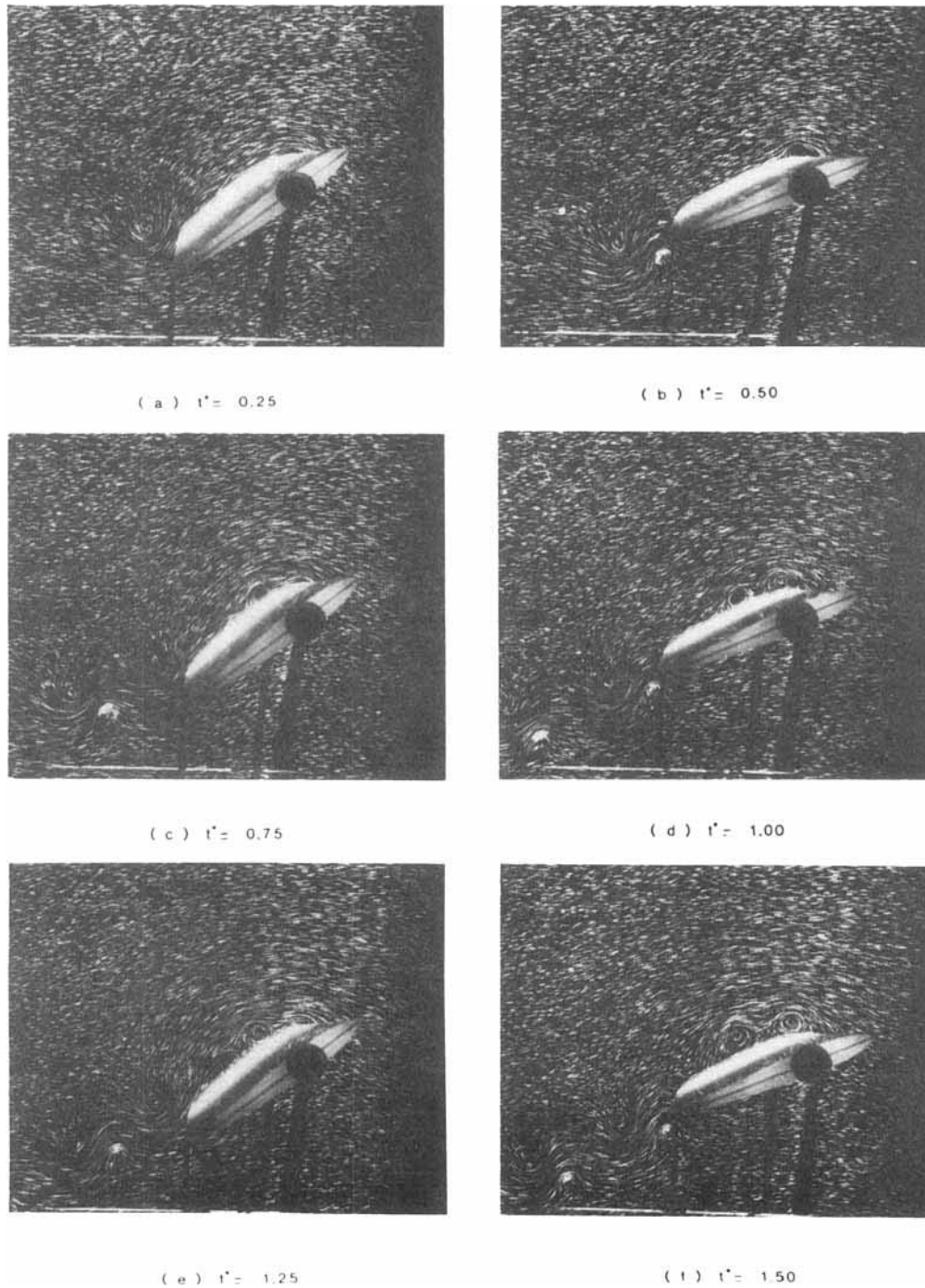

Figure 6(a)

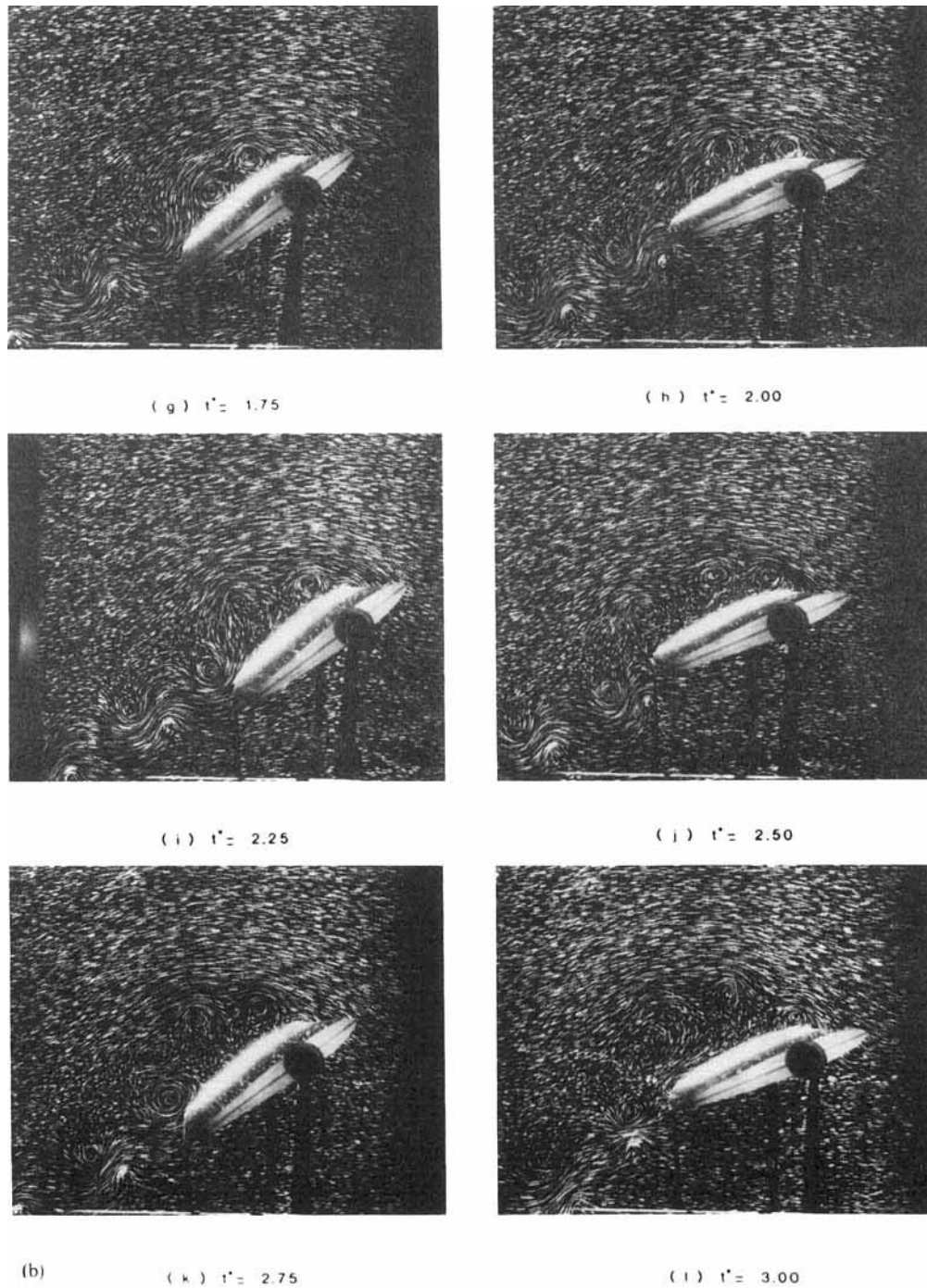

Figure 6. Time evolution of the flow structure; $Re = 3000, f^* = 1{\cdot}0, \alpha = 30^\circ, \Delta\alpha = -7^\circ, \alpha_0 = 23$

edge. As in the case $f^* = 0{\cdot}5$ the vortex shedding has the same frequency as the oscillaton motion of the aerofoil.

Experimental visualizations are presented in Figures 6(a) and 6(b), which numerical results are reported in Figures 7(a) and 7(b). Some discrepancies can be seen, in particular for $t^* > 3$. The flow structure becomes irregular and the tridimensional effects are no longer negligible.

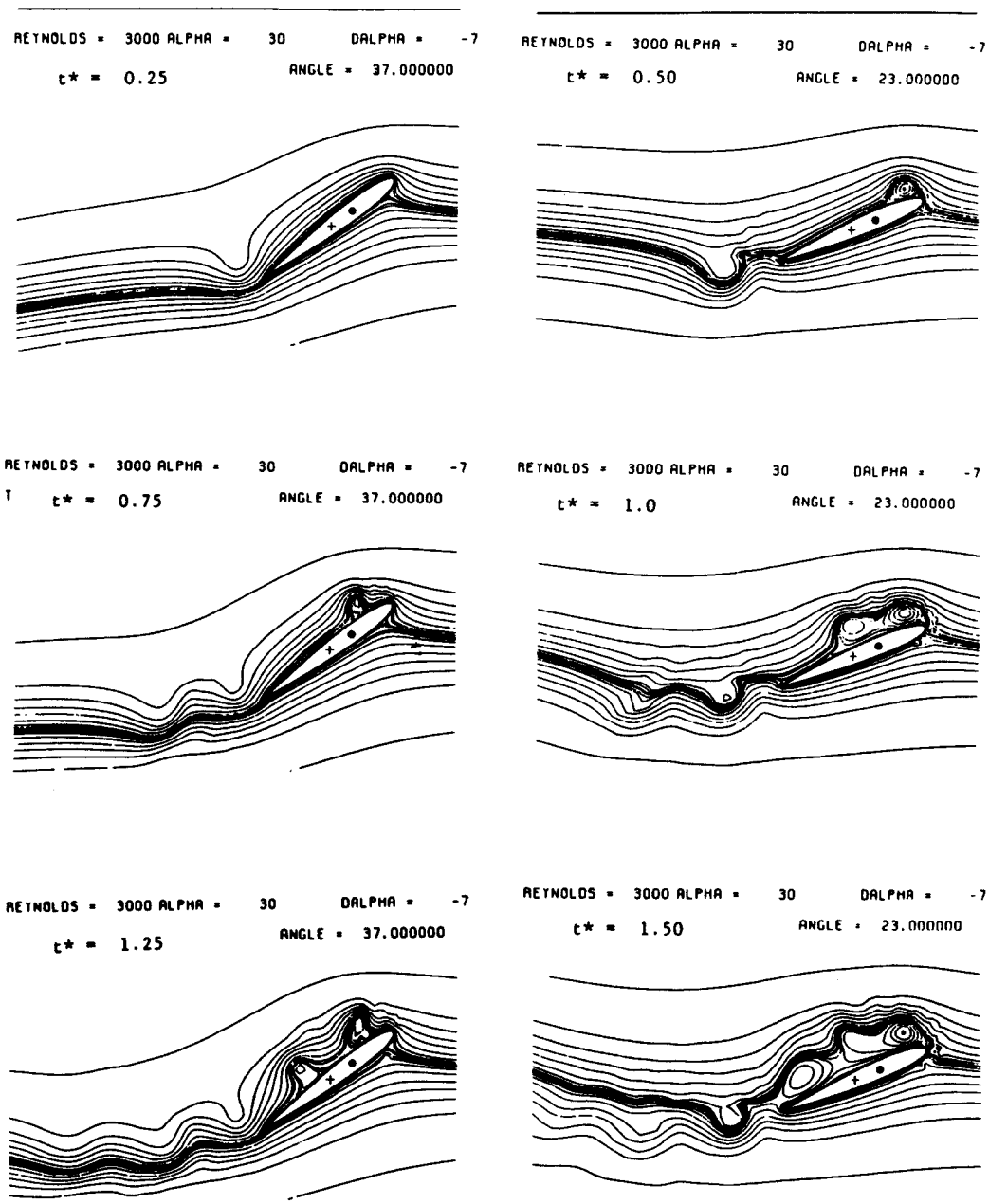

Figure 7(a)

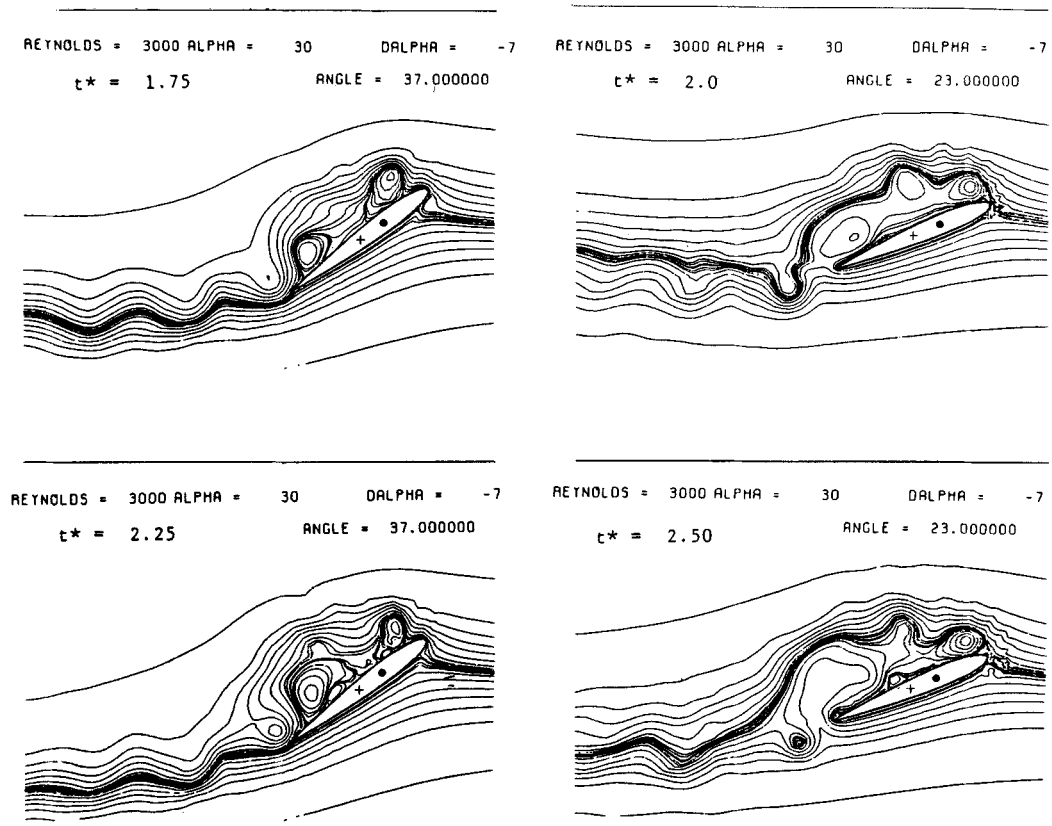

Figure 7. Time evolution of the flow structure; $Re = 3000, f^* = 1{\cdot}0, \alpha = 30°, \Delta\alpha = -7°, \xi_\infty = 0{\cdot}72324$

The calculations were carried out on an 81×121 grid and the time step was taken equal to 10^{-3}. These numerical and experimental analyses of the influence of the reduced frequency demonstrate that the vortex shedding frequency in the wake is the largest value between the natural frequency for the flow around an aerofoil with fixed incidence and the frequency of the oscillating motion.

Figure 8 gives an example of the drag (CX), lift (CY) and moment (CM) coefficients and shows the importance of hysteresis effects when dynamic deep stall cases are considered.

Influence of the amplitude of the oscillation. Two values of the amplitude and of the mean angle of attack will be considered here. It appears that the angular amplitude generally has a small influence on the formation and development of the vortex shedding. For a given frequency similar types of stall can be observed whatever the angular amplitude. A detailed analysis of these phenomena is reported in Ohmi.[9]

$Re = 10^4$

For this Reynolds number the reduced frequency f^* is always equal to 0·5. The mean value of the angle of attack was chosen to be 30° and the angular amplitude 7°. These low values allow us

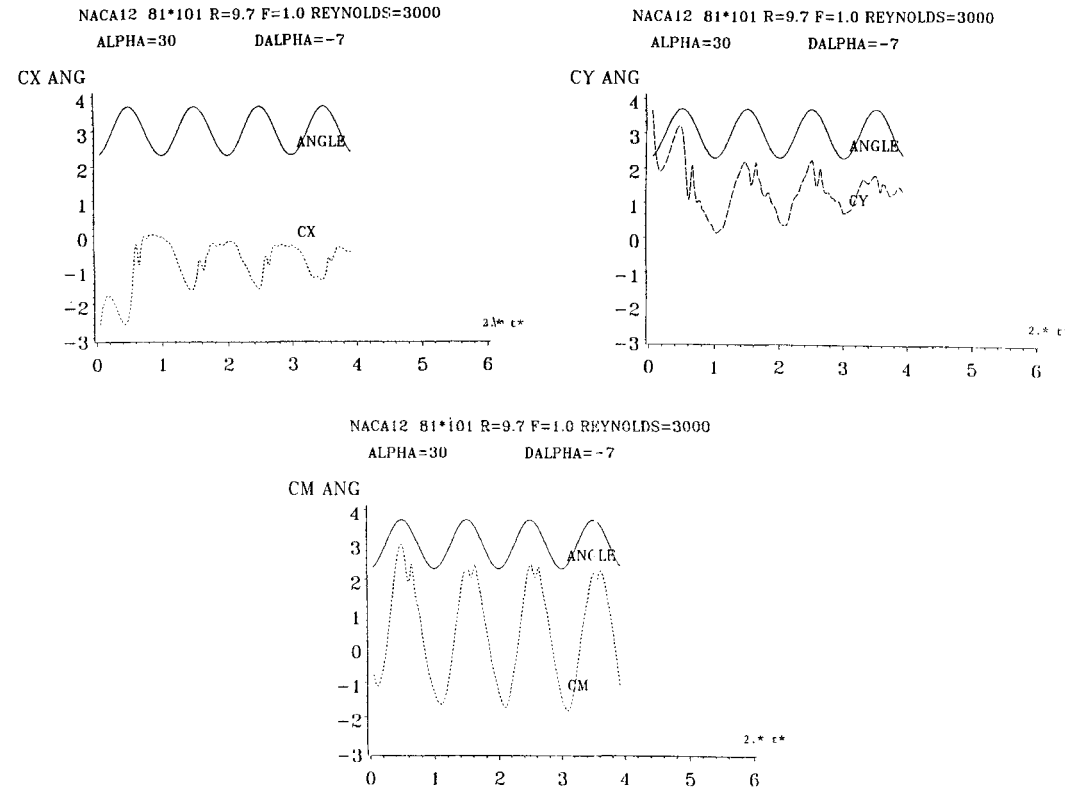

Figure 8. Evolution with time of the drag CX, lift CY and moment CM coefficients

to use a moderate number of nodes in the computations: a grid with 81×121 nodes and a time step equal to 10^{-3} were used. Comparison between numerical results (Figure 9(a)–9(c)) and experimental visualizations (Figures 10(a) and 10(b)) shows good agreement for t^* up to 4. However, it may be noticed that the vortices are slightly more developed in the experiments than in the numerical simulation.

CONCLUSIONS

Numerical and experimental results presented in this paper demonstrate that a numerical resolution of the unsteady Navier–Stokes equations is able to describe in a correct manner the flow generated by a simultaneously translating and pitching aerofoil. Analysis of the influence of the different parameters shows the following:

1. The Reynolds numbers considered in this paper do not have a major effect on the flow structure around the oscillating aerofoil but influence rather the phase lag and the hysteresis character of the wake.
2. The flow at $f^* = 0{\cdot}1$ is characterized by the upper surface flow generated during the two phases of increasing and decreasing incidence. The increase in incidence gives rise to an accelerated formation of secondary vortices which hastens the displacement and shedding of

leading edge vortices. The reduction of incidence produces trailing edge vortices which prevent the expansion of the viscous interaction area.

3. The flow at $f^* = 0{\cdot}5$ presents a rather stable vortex-shedding system at both leading and trailing edges. The leading edge throws out co-rotative vortices in a regular manner, probably because the rolling-up caused by the ascent of the leading edge is of the same dynamic scale as the natural growth of leading edge bubbles. The main interest of the flow

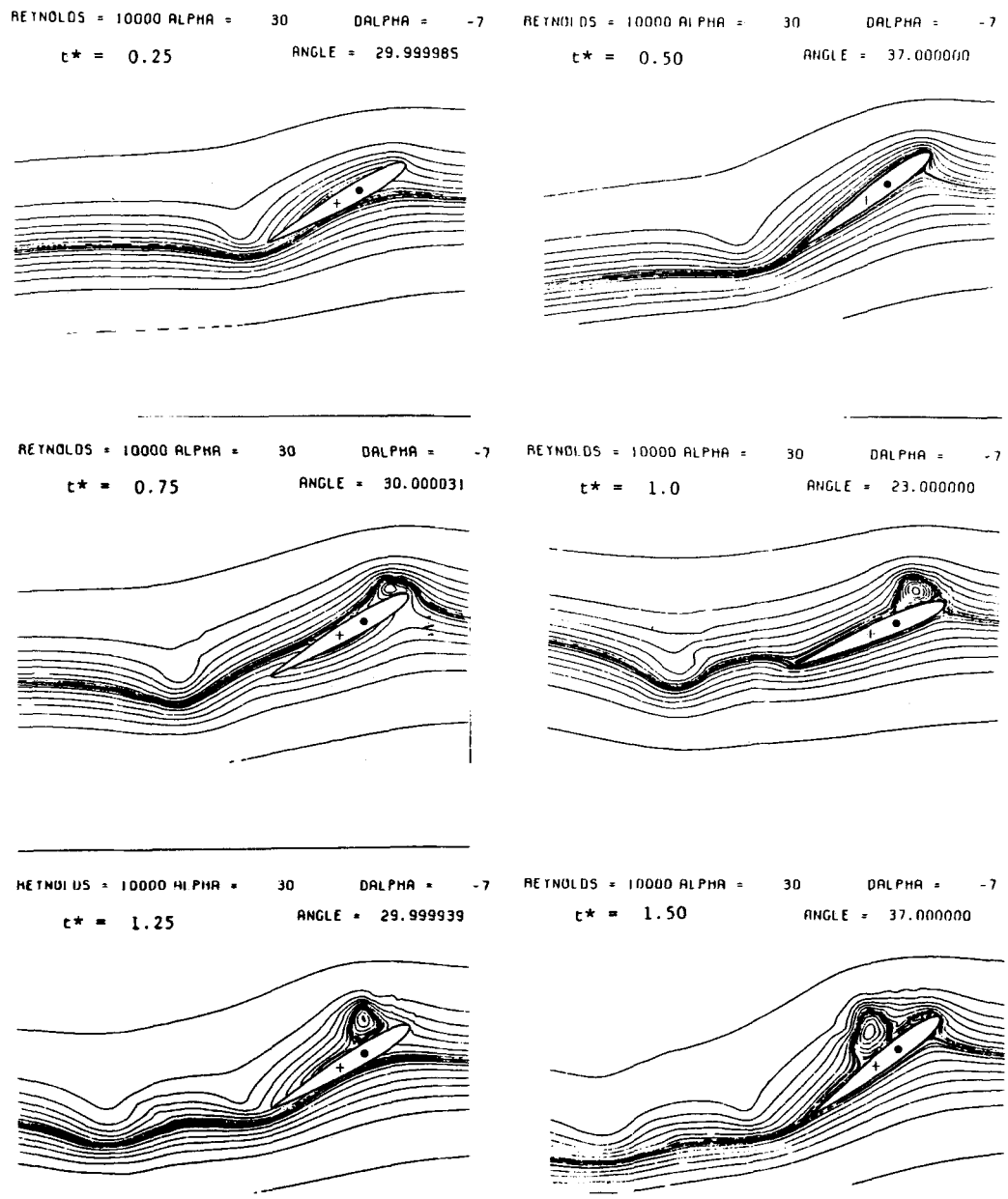

Figure 9(a)

features remains still in the upper surface flow, but one recognizes trailing edge vortices rolling up alternately into the upper surface and lower surface flows.

4. The main characteristic of the flow at $f^* = 1{\cdot}0$ is a strong rolling-up towards the upper surface flow which encloses completely the leading edge bubbles. The bubbles are then unable to grow normally with periodic supply of vorticity and instead form a single vortex

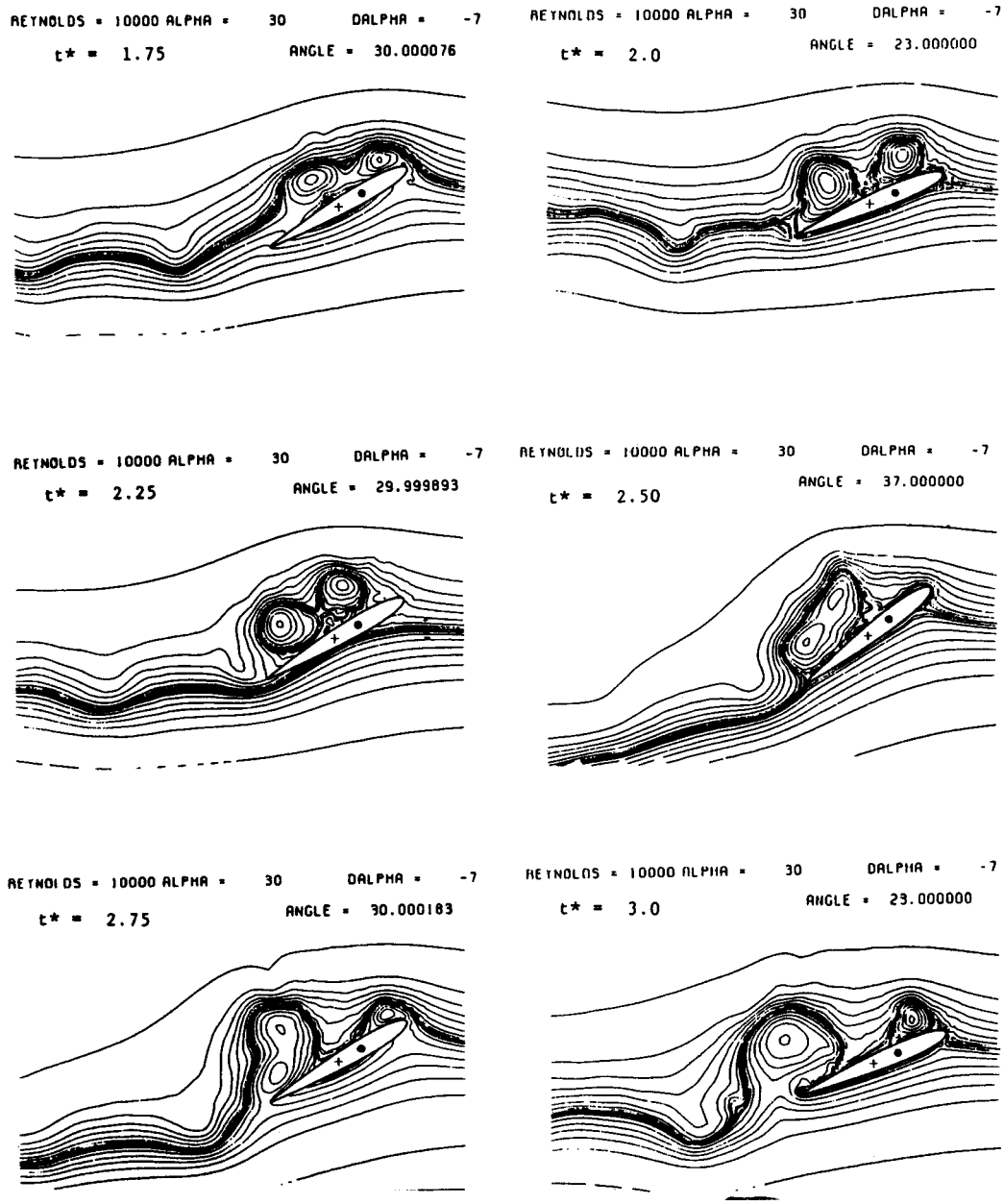

Figure 9(b)

cell which goes through gradual growth inside the enclosure. The strong rolling-up also causes a prominent flow reversal process which initiates from the leading edge and travels downstream.

5. The mean incidence and the angular amplitude of the oscillation do not have a definitive effect on the qualitative behaviour of the unsteady separation as long as the former remains clearly in excess of the static stall incidence. Nor is the maximal incidence a major factor

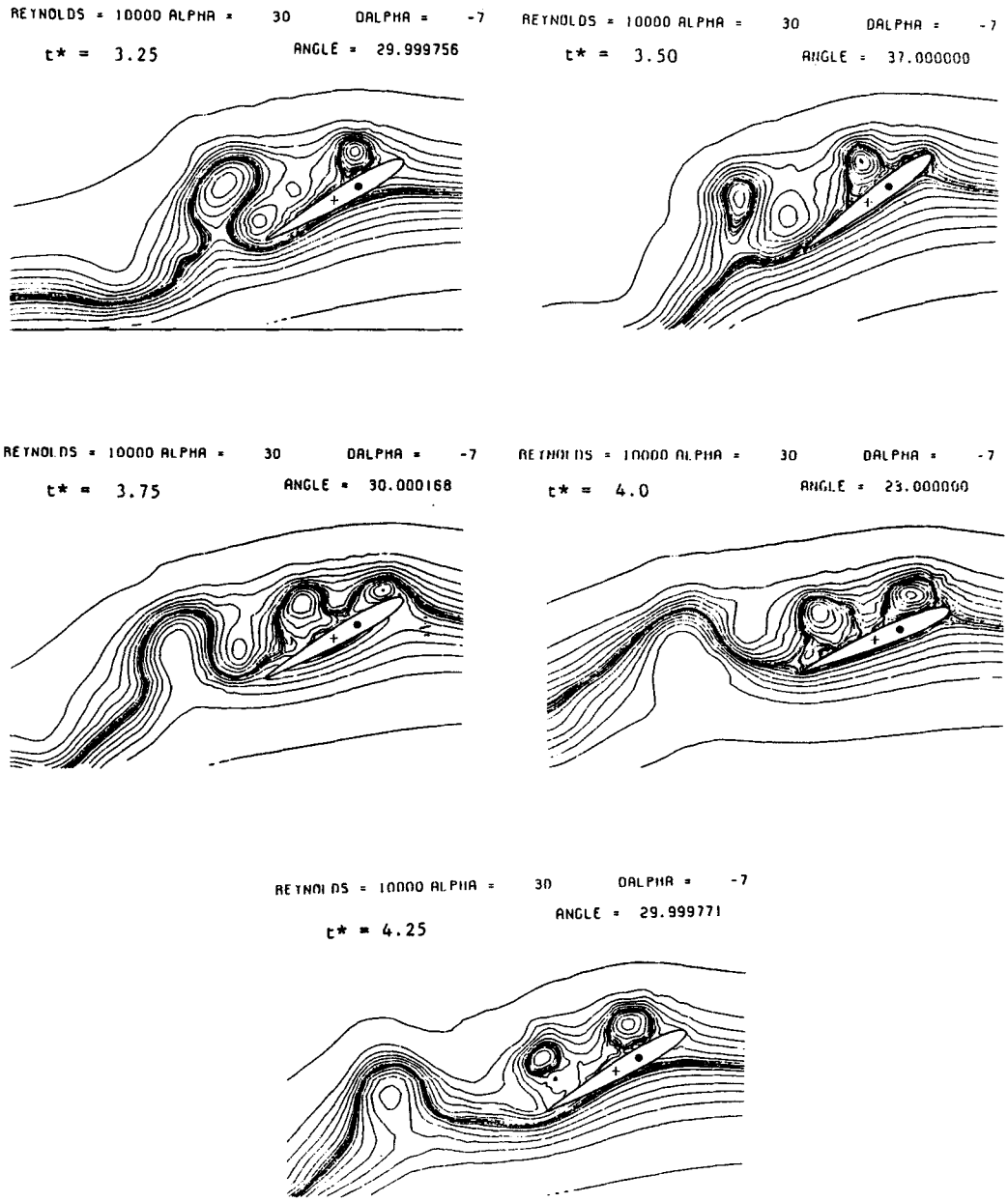

Figure 9. Time evolution of the flow structure; $Re = 10000$, $f^* = 0{\cdot}5$, $\alpha = 30°$, $\Delta\alpha = -7°$, $\xi_\infty = 0{\cdot}72324$

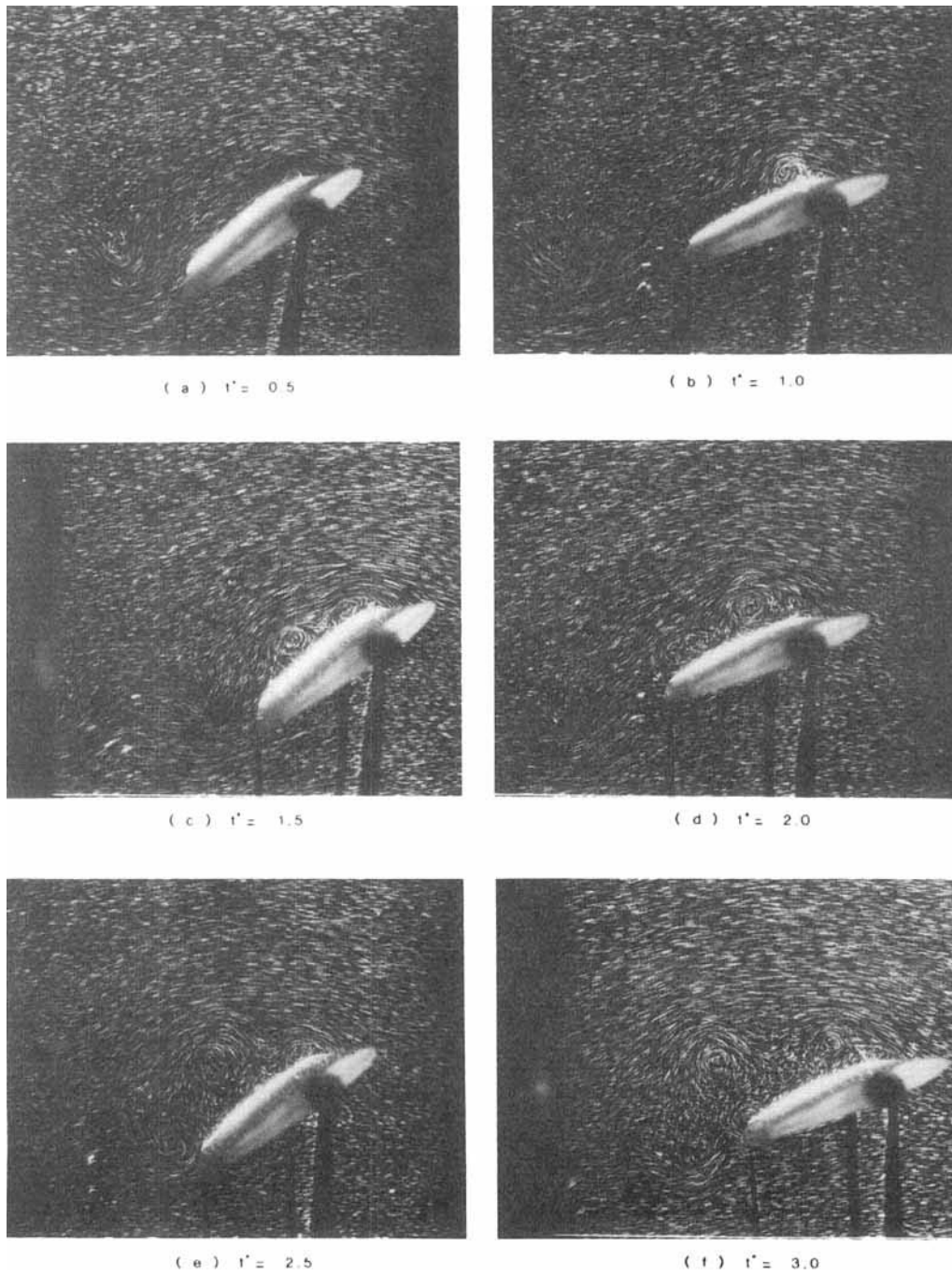

Figure 10(a)

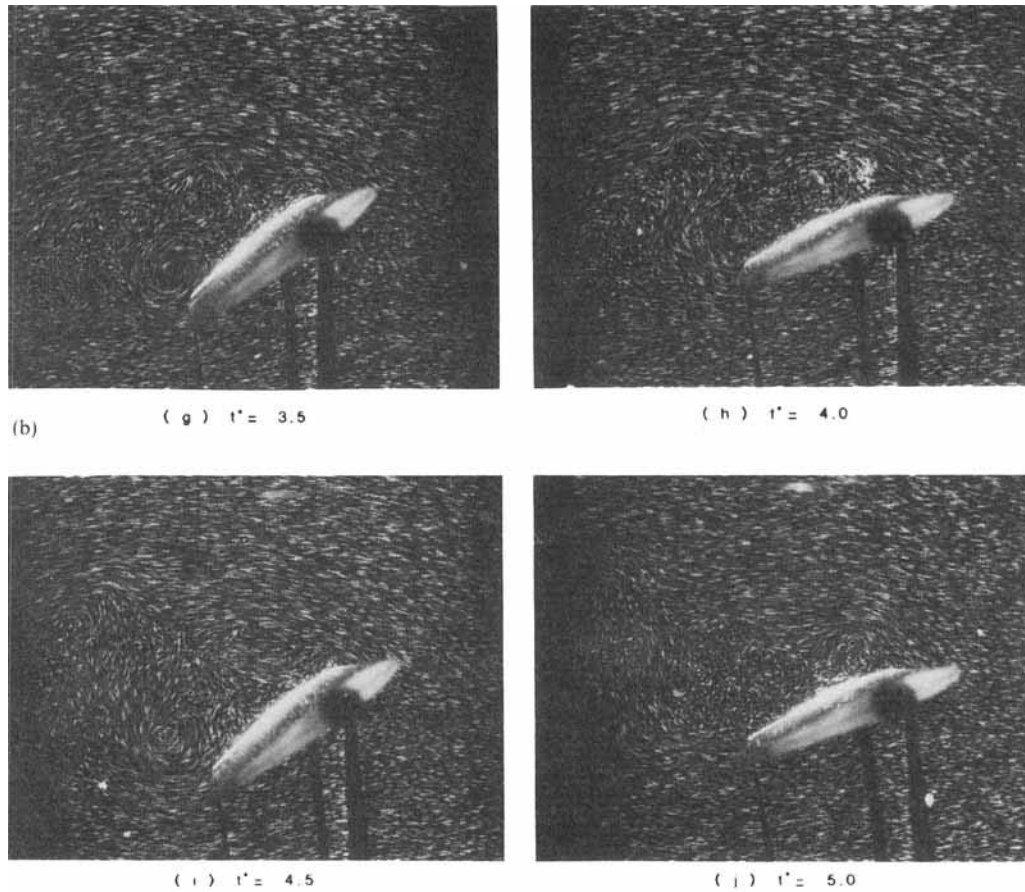

Figure 10. Time evolution of the flow structure; $Re = 10000$, $f^* = 0{\cdot}5$, $\alpha = 30°$, $\Delta\alpha = -7°$, $\alpha_0 = 23$

here. Needless to say, some quantitative estimates such as force coefficients and vorticity cannot be reached through visualizations and need some support from the numerical computations.

ACKNOWLEDGEMENT

This work was supported by the DRET of the French Ministry of Defence, under contract # 84.34.020.000

REFERENCES

1. N. D. Ham, 'Aerodynamic loading on a two-dimensional airfoil during dynamic stall', *AIAA J.*, **6,** 1927–1934 (1968).
2. J. M. Martin *et al.*, 'An experimental analysis of dynamic stall on an oscillating airfoil', *J. Amer. Helicopter Soc.*, **19,** 26–32 (1974).
3. N. Baudu, M. Sagner and J. Souquet, 'Modélisation du décrochage dynamique d'un profil oscillant', *AAAF 10eme Colloque d'Aérodynamique Appliquée*, Lille, 1973.
4. U. B. Metha, 'Dynamic stall of an oscillating airfoil', *AGARD CP-227, Paper 23,* 1977.
5. R. B. Kinney and Z. M. Cielak, 'Impulsive motion of an airfoil in a viscous fluid', in R. B. Kinney (ed.), *Symp. on Unsteady Aerodynamics*, University of Arizona, 1975, pp. 487–512.

6. J. C. Wu and S. Sampath, 'A numerical study of viscous flow around an airfoil', *AIAA Paper 76-337*, 1976.
7. H. Werlé and M. Gallon, *Note Technique 239*, ONERA, France, 1974.
8. K. Ohmi, M. Coutanceau, L. Ta Phuoc, O. Daube and A. Dulieu, 'Experimental and numerical visualizations of the flow past an impulsively started oscillating and translating elliptic cylinder', *4th Int. Symp. on Flow Visualization*, Paris, 1986.
9. K. Ohmi, 'Etude de la formation du sillage autour d'un profil en oscillation', *These*, Université de Poitiers, France, 1987.
10. L. W. Carr, K. W. McAllister and W. J. McCroskey, 'Analysis of the development of dynamic stall based on oscillating airfoil experiments', *NASA TN D-8382*, 1977.
11. L. Ta Phuoc and R. Bouard, 'Numerical solution of the early stage of the unsteady viscous flow around a circular cylinder', *J. Fluid Mech.*, **160**, 93–117 (1985).
12. H. J. Lugt and H. J. Haussling, 'Laminar flow past an abruptly accelerated elliptic cylinder at 45 degrees incidence', *J. Fluid Mech.*, **65**, 711–734 (1974).
13. L. Ta Phuoc and O. Daube, 'Higher order numerical solution of unsteady viscous flow generated by a transversely oscillating airfoil', *WAM ASME G00181*, 1980, pp. 155–171.
14. O. Daube, F. Niang and L. Ta Phuoc, 'Unsteady flow around a circular cylinder with suction', *4th Int. Conf. on Numerical Methods in Laminar and Turbulent Flows*, Swansea, 1985.
15. R. S. Hirsh, 'Higher order accurate difference solution of fluid mechanics problems by a compact differencing technique', *J. Comput. Phys.*, **19**, 90–100 (1975).
16. E. L. Wachspress, *Iterative Solutions of Elliptic Systems*, Prentice-Hall, Englewoods Cliffs, NJ, 1966.